UNIVERSITY OF COPENHAGEN
FACULTY OF SCIENCE

Master's thesis

Engineering superconducting qubits

From current state of the art superconducting qubits to the Flensmon

Anders Enevold Dahl

Advisor: Karsten Flensberg

Submitted: June 1, 2022

Abstract

This thesis gives an introduction to superconducting quantum bits (qubits). We will cover how qubits fail due to noise from an environment, and link coherence times to this noise. The coherence times are split up into depolarization and pure dephasing due to transverse and longitudinal noise. Circuit quantum electrodynamics (circuitQED) is introduced together with current qubits as examples.

The Flensmon qubit will be introduced and characterized by its coherence times and limitations. The Flensmon is a qubit with almost degenerate energy eigenvalues and well separated eigenstates. The limiting coherence time is found to be the pure dephasing due to flux noise. The gradiometric Flensmon is proposed where the dephasing time due to global flux noise is improved, however, the dephasing time due to local flux noise is still the limiting factor.

We will propose simple methods on how to manipulate and measure the Flensmon. Single qubit gates can be implemented by tuning a tunable Josephson junction to a regime where the qubit energies are split. Two Flensmons are capacitively coupled and used to make two qubit gates. We show how to turn on and off the overlap between eigenstates of the two qubit system. A dispersive readout is proposed. This technique is well known and is summarized.

Acknowledgments

I would like to thank my supervisor Karsten Flensberg for the last two years of my studies. First as a lecturer, then letting me do research at the condensed matter group, and lastly supervisor for my master's thesis. It has been instructive and fun all the way through. I would also like to mention Svend Krøjer Møller and thank him for all the time he spent discussing both physics and everyday life around the university. Without Svend, this project would not have come this far.

In realizing the theories we found at the Niels Bohr Building, Morten Kjærgaard has been invaluable in discussing all the experimental aspects of superconducting qubits. For the last three months, Kasper Sangild Christensen visited the Niels Bohr institute from Aarhus University, and with an experience in superconducting circuits, we all benefited greatly from.

Furthermore, I would like to thank the whole condensed matter group for having me for the last two years, where I have been around the CMT tower. It has been a pleasure with the guys from the office the past nine months, here I would especially like to thank Emil Hellebek for the early mornings, late evenings, and everything in between where the spirits always were kept high.

Finally, thanks to all my friends who kept with me even though I have been busy at times. Thanks to the people I have lived with at Rigshospitalets Kollegium and all the fellow physics students I have met during my studies.

Contents

Chapter 1

Introduction

In May 1981, Richard Feynman claimed that classical computers, as we know them with classical bits, will not be able to simulate quantum systems [1]. He reasoned that to simulate nature, a computer should consist of the same nature [2] e.g., to simulate a quantum system one would need a quantum computer. Feynman was one of the first physicists to argue that a quantum computer would be able to solve problems we are not able to solve with classical computers. Now we know that not only quantum mechanical problems, but also classical problems where we do not have enough computer power, can be solved quickly on a quantum computer. Problems can be categorized into complexity classes:

- P - Problems that can be solved in polynomial time on a classical computer.
- NP - Problems that cannot be solved in polynomial time on a classical computer, but the answer can be verified in polynomial time.

Asking whether a number is a prime is a P problem, but finding the prime factors of a number is an NP problem, however the prime factors can easily be verified. This is a typical example of how a quantum computer can break classical encryption, as this is based on prime factorization. Peter Shor was the first to make a prime factorization algorithm for a quantum computer [3].

In the medical and pharmaceutical industry, a lot of computer power is used to simulate molecules, but molecules often become complicated fast, and even small well-known molecules like caffeine are hard and time-consuming to simulate on a classical computer. A quantum computer would be more efficient in predicting new molecules used for medication [4]. These are just some of the many applications of quantum computation.

A classical computer is operated by bits, which are either 0 or 1. These are often transistors that are on or off. A quantum computer is built of quantum

mechanical systems, called quantum bits (qubits), acting as quantum transistors with the eigenstates $|0\rangle$ and $|1\rangle$, where the wave function, $|\psi\rangle$, can take any superposition $|\psi\rangle = \alpha\,|0\rangle + \beta\,|1\rangle$, where α and β are probability amplitudes. There is a wide variety of ideas on how to build qubits: any quantum mechanical two level system could be a good candidate. Popular candidates are superconducting circuits, ion traps [5], photon polarization [6], or any other quantum system, which can be reduced to two levels.

What is a qubit?

A common way of representing a qubit state is in the Bloch sphere. The probability amplitudes in this representation is $\alpha = \cos\frac{\theta}{2}$ and $\beta = e^{i\phi}\sin\frac{\theta}{2}$, where, θ, the projection on the z-axis which tells the superposition, and the azimuthal angle, ϕ, is the phase, as depicted in Figure 1.1.

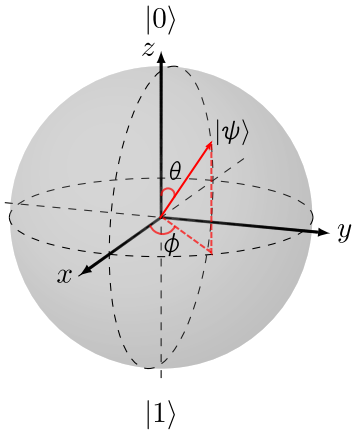

Figure 1.1: The qubit state, $|\psi\rangle$, is represented as a point on the surface of a unit sphere called the Bloch sphere. The state is described by the projection on the z-axis, θ, and the azimuthal angle, ϕ.

It can be hard to engineer a "pure" two level system, it is often enough to make an isolated subspace of two levels in the quantum system. Sometimes the higher levels are used as virtual transitions for qubit manipulations.

A superconducting qubit can be realized by using superconductors to construct electronic circuits. These are often operated at very low temperatures. Qubits are often controlled by applied magnetic fields or gate voltages to change the superconducting phase or the number of electrons in the system.

Building a quantum computer can be a great challenge. DiVincenzo described how realizing a quantum computer could be done by fulfilling five criteria [7]:

1. A scalable physical system with well characterized qubits.
2. The ability to initialize the state of the qubits to a simple fiducial state, such as $|000\ldots\rangle$.
3. Long relevant decoherence times, much longer than the gate operation times.
4. A "universal" set of quantum gates.
5. A qubit-specific measurement capability.

Systems that fulfill some of these criteria have been realized, but they often have a problem with one or more of the other criteria. The challenge lies in protecting the qubit from the environment, but still being able to manipulate and measure the qubit. Long coherence times are often a challenge, as the environment around always interacts with the qubit. To manipulate and measure the qubit, controlled interaction with the qubit is needed.

Superconducting qubits are one of the more promising candidates for a large-scale quantum computer. Several superconducting qubits have already been realized, but are not robust enough, as they are subject to decoherence by interactions from the surrounding environment. There are three common ways to make the qubit less susceptible to interactions. An option is to filter noise away, such that the environment does not interfere with the qubit. Another option is quantum error correction, where one correct for possible errors when quantum algorithms are executed. Lastly one could engineer a qubit, which is not affected by noise in the external parameters from the surrounding environment [8].

Google [9] and IBM [10] are some of the big companies that are combining several superconducting qubits into a quantum computer. Both companies use the well-known Transmon qubit [11], however, there is still a lot of noise in the current large-scale quantum computers. To get a better working quantum computer, new and better qubits are needed, with longer coherence times and faster gates.

Outline

In this thesis, we will work with a superconducting circuit to construct a two level system, which we can use for a qubit. To construct a good qubit we need a system that does not decohere, a system which we can manipulate e.g. do gates and readout. We will introduce a new proposal for a superconducting qubit. It has the

same topology as the old persistent-current flux qubit [12], and the newer capacitively shunted flux qubit [13], but it is operated in another parameter regime. We will call this new qubit the Flensmon. We will characterize the qubit, but before we propose the new qubit, it will be worked through how a general two level system can break because of decoherence. Chapter 2 focuses on a two level system where there is noise in the external parameters in the Hamiltonian. In Chapter 3, we give an overview of circuit quantum electrodynamics (circuitQED), here we show how to derive a Hamiltonian from a quantum circuit. Here the Transmon is also introduced. The Flensmon is introduced in Chapter 4, where the circuit is shown. The Hamiltonian is set up and solved numerically in order to estimate coherence times. Like most flux qubits, the Flensmon is sensitive to flux noise [14]. In Chapter 5, we try to engineer the circuit to be less sensitive to flux noise, without changing the properties of the qubit. In Chapter 6, we discuss first how to manipulate our proposed qubit with simple single and two qubit gates. Briefly, Chapter 7 mentions methods of readout of the system. Last, in Chapter 8, we conclude the thesis and present an outlook for future work.

Chapter 2

Coherence of Qubits

The coherence time for a qubit is essential for making a working quantum computer. If the lifetime of a qubit is too short, it can be hard to operate and manipulate the qubit, as the time one has to do operations is limited by this characteristic time.

The two level system making out the qubit is subject to interactions with the surrounding environment. To characterize a qubit, the total decoherence is often measured. This chapter is about how we can estimate the decoherence of a qubit. The total decoherence rate can be split up into depolarization rate and pure dephasing rate [15, 16]. Depolarization rates and pure dephasing are depicted in Figure 2.1.

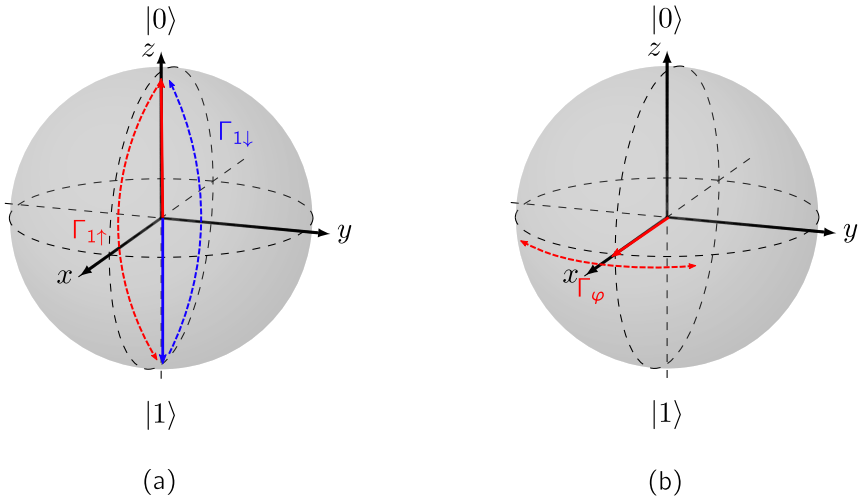

Figure 2.1: Bloch sphere representation of transition rates. (a) Depolarization rate due to transverse noise driving $|0\rangle \leftrightarrow |1\rangle$ transitions. Excitations are suppressed in the low temperature limit. (b) Pure dephasing rate due to longitudinal noise in the xy-plane fluctuating the qubit frequency.

Transverse noise drives transitions between $|0\rangle$ and $|1\rangle$. Excitations are often suppressed by performing experiments at low temperatures, $\Gamma_1 = \Gamma_{1\downarrow} + \Gamma_{1\uparrow} \approx \Gamma_{1\downarrow}$. The relaxation rate $\Gamma_{1\downarrow}$ is thus the depolarization rate. Longitudinal noise gives rise to dephasing in the xy-plane. This fluctuates the qubit frequency as we will see in the derivation for the dephasing time. The two noise channels characterize two decoherence times:

$$\text{Depolarization time:} \quad T_1 = \frac{1}{\Gamma_1}, \tag{2.1}$$

$$\text{Pure dephasing time:} \quad T_\varphi = \frac{1}{\Gamma_\varphi}, \tag{2.2}$$

together this characterizes the total decoherence of the system [15, 16],

$$\text{Total decoherence time:} \quad T_2 = \frac{1}{\frac{\Gamma_1}{2} + \Gamma_\varphi}. \tag{2.3}$$

In this chapter, we will derive the pure dephasing and depolarization time produced by small fluctuations in the external parameters of the Hamiltonian.

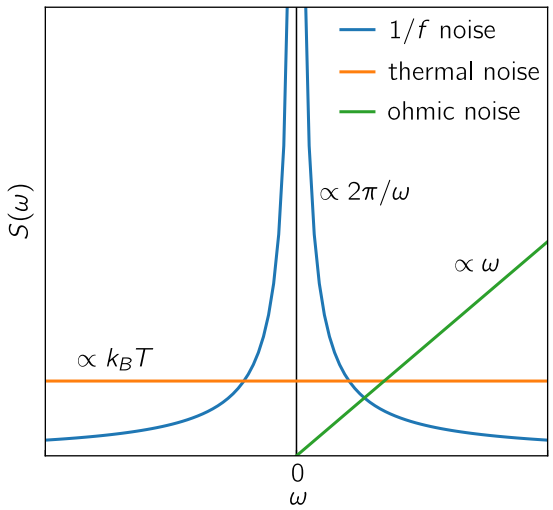

Figure 2.2: Power spectral function for different noise types. The blue curve is $1/f$ noise which is dominant at low frequencies. The orange curve is thermal noise, this often causes excitations. The green curve is ohmic noise which dominates at higher frequencies. Figure inspired from [15].

Noise in the external parameters is drawn from a distribution and has a power spectral density which is the Fourier transform of the autocorrelation function,

$$S(\omega) = \int_{-\infty}^{\infty} \mathrm{d}t \; \mathrm{e}^{-i\omega t} \left\langle \delta\lambda(t)\delta\lambda(0) \right\rangle . \tag{2.4}$$

Different power spectral functions arise for different kinds of noise. Figure 2.2 shows the power spectral functions for $1/f$ noise, thermal noise, and ohmic noise. The relevant power spectral function depends on the frequency the system is operated at. At low frequencies, $1/f$ noise dominates, while at higher frequencies ohmic noise dominate. We work in the low temperature limit and will not focus on thermal noise. If the noise is classical, the power spectral density will be symmetric in frequency space, as the autocorrelation function of classical signals is real. Quantum systems can have an imaginary autocorrelation function and the power spectral function will be asymmetric [15].

Pure dephasing time

The following derivation is inspired by appendix A in [17]. We look at an external parameter $\lambda = \lambda_0 + \delta\lambda(t)$, λ could be flux, charge or another external parameter. $\delta\lambda(t)$ is classical noise arising from a Gaussian process with mean $\langle\delta\lambda(t)\rangle = 0$, and noise power spectrum $S(\omega) = \int_{-\infty}^{\infty} \mathrm{d}t\ \mathrm{e}^{-i\omega t} \langle\delta\lambda(t)\delta\lambda(0)\rangle$. The Hamiltonian depends on the external parameter, and we assume that the effect of the noise is sufficiently small to allow a Taylor expansion in $\delta\lambda$,

$$\mathcal{H} = \mathcal{H}(\lambda_0) + \frac{\partial\mathcal{H}}{\partial\lambda}\bigg|_{\lambda_0} \delta\lambda(t) + \frac{1}{2}\frac{\partial^2\mathcal{H}}{\partial\lambda^2}\bigg|_{\lambda_0} \delta\lambda^2(t) + \mathcal{O}\big(\delta\lambda^3\big) \approx H_0 + V_\lambda(t), \tag{2.5}$$

where we define $H_0 = \mathcal{H}(\lambda_0)$ and $V_\lambda(t) = \frac{\partial\mathcal{H}}{\partial\lambda}\big|_{\lambda_0} \delta\lambda(t) + \frac{1}{2}\frac{\partial^2\mathcal{H}}{\partial\lambda^2}\big|_{\lambda_0} \delta\lambda^2(t)$. Throughout this section we evaluate the derivatives with respect to λ in $\lambda = \lambda_0$. It is convenient to switch to the interaction picture. The usual transformations for states is $\big|\bar{\psi}(t)\big\rangle = \mathrm{e}^{iH_0t}\,|\psi(t)\rangle$ and operators $\bar{X} = \mathrm{e}^{iH_0t}X\mathrm{e}^{-iH_0t}$. The eigenbasis $|n\rangle$ of H_0 is used to express $\big|\bar{\psi}(t)\big\rangle$ in terms of probability amplitudes $c_n(t) = \big\langle n\big|\bar{\psi}(t)\big\rangle$. The time-dependent Schrödinger equation in the interaction picture is then (with $\hbar = 1$),

$$i\frac{\mathrm{d}}{\mathrm{d}t}\big|\bar{\psi}(t)\big\rangle = \bar{V}_\lambda(t)\big|\bar{\psi}(t)\big\rangle \Leftrightarrow i\frac{\mathrm{d}}{\mathrm{d}t}c_n(t) = \langle n|\,\bar{V}_\lambda(t)\big|\bar{\psi}(t)\big\rangle = \sum_{n'}\langle n|\,\bar{V}_\lambda(t)\,|n'\rangle\,c_{n'(t)}. \tag{2.6}$$

From Equation (2.5), $\bar{V}_\lambda(t)$ is a noise operator in the interaction picture. In general, this operator can be written in longitudinal and transverse terms,

$$\bar{V_\lambda}(t) = \sum_n v_n(t) \left|n\right\rangle \left\langle n\right| + \sum_{n \neq m} v_{n,m}(t) \left|n\right\rangle \left\langle m\right|, \tag{2.7}$$

where the first term is responsible for pure dephasing as there are no transitions between different states, while the second term is responsible for depolarization. In this section, we are only interested in pure dephasing hence the transverse terms are ignored. The time-dependent Schrödinger equation is written where the transverse terms are ignored,

$$i\frac{\mathrm{d}}{\mathrm{d}t}c_n(t) = \sum_{n',m} v_m(t) \left\langle n|m\right\rangle \left\langle m|n'\right\rangle c_{n'}(t) = v_n(t)c_n(t), \tag{2.8}$$

the differential equation is easily solved,

$$c_n(t) = \exp\left[-i\int_0^t \mathrm{d}t\, v_n(t')\right] \Leftrightarrow \left|\bar{\psi}_n(t)\right\rangle = \exp\left[-i\int_0^t \mathrm{d}t'\, v_n(t')\right] \left|n\right\rangle, \tag{2.9}$$

as expected, the longitudinal terms only affect the phase of the state. Using the noise operator in Equation (2.7) and the Hamiltonian decomposition in Equation (2.5) we find,

$$\begin{aligned} v_n(t) &= \left\langle n\right| \bar{V_\lambda}(t) \left|n\right\rangle = \left\langle n\right| \mathrm{e}^{iH_0t} V_\lambda(t) \mathrm{e}^{-iH_0t} \left|n\right\rangle = \left\langle n\right| \mathrm{e}^{iE_{0,n}t} V_\lambda(t) \mathrm{e}^{-iE_{0,n}t} \left|n\right\rangle \\ &= \left\langle n\right| V_\lambda \left|n\right\rangle = \left\langle n\right| \partial_\lambda \mathcal{H} \left|n\right\rangle \delta\lambda(t) + \frac{1}{2} \left\langle n\right| \partial_\lambda^2 \mathcal{H} \left|n\right\rangle \delta\lambda^2(t) \\ &= d_n \delta\lambda(t) + \frac{1}{2} D_n \delta\lambda^2(t), \end{aligned} \tag{2.10}$$

where $d_n = \left\langle n\right| \partial_\lambda \mathcal{H} \left|n\right\rangle$ and $D_n = \left\langle n\right| \partial_\lambda^2 \mathcal{H} \left|n\right\rangle$. We calculate the first and second order coefficients d_n and D_n with $\mathcal{H} = \sum_m E_m(\lambda) \left|m(\lambda)\right\rangle \left\langle m(\lambda)\right|$,

$$\begin{aligned} d_n &= \left\langle n\right| \partial_\lambda \left(\sum_m E_m(\lambda) \left|m(\lambda)\right\rangle \left\langle m(\lambda)\right| \right) \left|n\right\rangle \\ &= \partial_\lambda E_n(\lambda) + E_n(\lambda_0) \left(\left\langle n\right| \partial_\lambda \left|n(\lambda)\right\rangle + \partial_\lambda \left\langle n(\lambda)|n\right\rangle \right) \\ &= \partial_\lambda E_n(\lambda) + E_n(\lambda_0) \left(\left\langle n\right| \partial_\lambda \left|n(\lambda)\right\rangle - \left\langle n\right| \partial_\lambda \left|n(\lambda)\right\rangle \right) = \partial_\lambda E_n, \end{aligned} \tag{2.11}$$

and by similar approach the second order coefficient are,

$$D_n = \left\langle n\right| \partial_\lambda^2 \mathcal{H} \left|n\right\rangle = \partial_\lambda^2 E_n. \tag{2.12}$$

Inserting v_n into Equation (2.9),

$$\left|\bar{\psi}_n(t)\right\rangle = \exp\left[-i\partial_\lambda E_n \int_0^t \mathrm{d}t'\, \delta\lambda(t') - \frac{i}{2}\partial_\lambda^2 E_n \int_0^t \mathrm{d}t'\, \delta\lambda^2(t')\right] |n\rangle\,. \tag{2.13}$$

From a Ramsey-type experiment the pure dephasing times can be extracted. Starting in an initial superposition $\left|\bar{\psi(0)}\right\rangle = \frac{1}{\sqrt{2}}(|0\rangle + |1\rangle)$, we wish to find the time evolved state. We have just derived how the number states time evolve, hence we can write the state,

$$\left|\bar{\psi}(t)\right\rangle = \frac{1}{\sqrt{2}}\left(\left|\bar{\psi}_0(t)\right\rangle + \left|\bar{\psi}_1(t)\right\rangle\right) = \frac{1}{\sqrt{2}}(\rho_0(t)\,|0\rangle + \rho_1(t)\,|1\rangle), \tag{2.14}$$

where $\rho_n(t) = \exp\left[-i\partial_\lambda E_n \int_0^t \mathrm{d}t'\, \delta\lambda(t') - \frac{i}{2}\partial_\lambda^2 E_n \int_0^t \mathrm{d}t'\, \delta\lambda^2(t')\right]$. The corresposnding 2×2 density matrix is,

$$\rho(t) = \frac{1}{2}\begin{pmatrix} \rho_{00}(t) & \rho_{01}(t) \\ \rho_{10}(t) & \rho_{11}(t) \end{pmatrix}, \tag{2.15}$$

where $\rho_{nm}(t) = \rho_n^*(t)\rho_m(t)$, so the coefficients are,

$$\begin{aligned} &\rho_{00} = \rho_{11} = 1, \\ &\rho_{10} = \rho_{01}^*, \\ &\rho_{01} = \exp\left[-i\partial_\lambda \omega_q \int_0^t \mathrm{d}t'\, \delta\lambda(t') - \frac{i}{2}\partial_\lambda^2 \omega_q \int_0^t \mathrm{d}t'\, \delta\lambda^2(t')\right], \end{aligned} \tag{2.16}$$

where $\omega_{01} = E_1 - E_0$. It is the off diagonal elements in $\rho(t)$ which we can extract the dephasing time from. Averaging over time in the limit where we wait infinitely long time $\lim_{t\to\infty} \langle\rho_{01}\rangle\,(t) = 0$, this often occurs at a characteristic timescale T_φ. We write $\rho_{01} = \mathrm{e}^{iY}$. The average is approximated by $\left\langle \mathrm{e}^{iY} \right\rangle \approx \mathrm{e}^{i\langle Y\rangle}\mathrm{e}^{-\frac{i}{2}\left(\left\langle Y^2\right\rangle - \langle Y\rangle^2\right)}$, as we have kept terms up to second order in $\delta\lambda(t)$ again.

$$\begin{aligned} Y &= \partial_\lambda \omega_q \int_0^t \mathrm{d}t'\, \delta\lambda(t') - \frac{1}{2}\partial^2 \lambda \omega_q \int_0^t \mathrm{d}t'\, \delta\lambda^2(t') \\ Y^2 &= (\partial_\lambda \omega_q)^2 \int_0^t \mathrm{d}t_1 \int_0^t \mathrm{d}t_2\, \delta\lambda(t_1)\delta\lambda(t_2) + \frac{1}{4}\left(\partial_\lambda^2 \omega_q\right)^2 \int_0^t \mathrm{d}t_1 \int_0^t \mathrm{d}t_2\, \delta\lambda^2(t_1)\delta\lambda^2(t_2) \\ &\quad + (\partial_\lambda \omega_q)\left(\partial_\lambda^2 \omega_q\right) \int_0^t \mathrm{d}t_1 \int_0^t \mathrm{d}t_2\, \delta\lambda(t_1)\delta\lambda^2(t_2). \end{aligned} \tag{2.17}$$

Now we take the expectation value, where we remember that $\langle \delta\lambda(t) \rangle = 0$ while $\langle \delta\lambda^2(t) \rangle \neq 0$. The cross terms in Y^2 has an average 0 as they are odd,

$$\begin{aligned}
\langle Y \rangle &= -\frac{1}{2}\partial_\lambda^2 \omega_q \int_0^t \mathrm{d}t' \ \langle \delta\lambda(0)\delta\lambda(0) \rangle \\
\left\langle Y^2 \right\rangle &= (\partial_\lambda \omega_q)^2 \int_0^t \mathrm{d}t_1 \int_0^t \mathrm{d}t_2 \ \langle \delta\lambda(t_2 - t_1)\delta\lambda(0) \rangle \\
&\quad + \frac{1}{4}\left(\partial_\lambda^2 \omega_q\right)^2 \int_0^t \mathrm{d}t_1 \int_0^t \mathrm{d}t_2 \ \left\langle \delta\lambda^2(t_2 - t_1)\delta\lambda^2(0) \right\rangle \qquad (2.18) \\
&= (\partial_\lambda \omega_q)^2 \int_0^t \mathrm{d}t_1 \int_0^t \mathrm{d}t_2 \ \langle \delta\lambda(t_2 - t_1)\delta\lambda(0) \rangle \\
&\quad + \langle Y \rangle^2 + \frac{1}{2}\left(\partial_\lambda^2 \omega_q\right)^2 \int_0^t \mathrm{d}t_1 \int_0^t \mathrm{d}t_2 \ \langle \delta\lambda(t_2 - t_1)\delta\lambda(0) \rangle^2 , \qquad (2.19)
\end{aligned}$$

where for the second order expression in $\langle Y^2 \rangle$, Wick's theorem is applied $\langle \delta\lambda^2(t_2 - t_1)\delta\lambda^2(0) \rangle = \langle \delta\lambda(0)\delta\lambda(0) \rangle^2 + 2 \langle \delta\lambda(t_2 - t_1)\delta\lambda(0) \rangle^2$ between Equation (2.18) and Equation (2.19) and noting $\langle \delta\lambda^2(t_2 - t_1) \rangle^2 = \langle \delta\lambda^2(0) \rangle^2$. We then have to solve two integrals,

$$\begin{aligned}
I_1 &= \int_0^t \mathrm{d}t_1 \int_0^t \mathrm{d}t_2 \ \langle \delta\lambda(t_2 - t_1)\delta\lambda(0) \rangle , \\
&= 4 \int_{-\infty}^{\infty} \frac{\mathrm{d}\omega}{2\pi} \frac{S_\lambda(\omega)}{\omega^2} \sin^2\left(\frac{\omega t}{2}\right), \qquad (2.20)
\end{aligned}$$

where the inverse Fourier transform, $\langle \delta\lambda(t)\delta\lambda(0) \rangle = \int_{-\infty}^{\infty} \frac{\mathrm{d}\omega}{2\pi} \, \mathrm{e}^{i\omega t} S_\lambda(\omega)$, is used.

$$\begin{aligned}
I_2 &= \int_0^t \mathrm{d}t_1 \int_0^t \mathrm{d}t_2 \, \langle \delta\lambda(t_2 - t_1)\delta\lambda(0) \rangle^2 , \\
&= 4 \int_{-\infty}^{\infty} \frac{\mathrm{d}\omega}{2\pi} \int_{-\infty}^{\infty} \frac{\mathrm{d}\Omega}{2\pi} \frac{S_\lambda(\omega) S_\lambda(\Omega)}{(\omega + \Omega)^2} \sin^2\left(\frac{(\omega + \Omega)t}{2}\right). \qquad (2.21)
\end{aligned}$$

To evaluate the integral and get an estimate for the dephasing time, we need to pick a power spectrum. For this analysis the power spectrum for $1/f$ noise is used $S_\lambda(\omega) = \frac{2\pi A_\lambda^2}{|\omega|}$, then the integrals evaluate to

$$I_1 = 2A_\lambda^2 |\ln(\omega_{ir} t)| t^2 \qquad (2.22)$$

$$I_2 = 4A_\lambda^4 \ln^2(\omega_{ir} t) t^2, \qquad (2.23)$$

whereby hand we have defined a lower bound of the frequency, ω_{ir}, for the integral not to diverge. The average of Equation (2.16) is then,

$$\langle \rho_{01} \rangle (t) \approx \exp[i \langle Y \rangle] \exp\Big[-\Big\{ A_\lambda^2 (\partial_\lambda \omega_q)^2 |\ln(\omega_{ir} t)| + A_\lambda^4 \big(\partial_\lambda^2 \omega_q\big)^2 \ln^2(\omega_{ir} t) \Big\} t^2 \Big] \quad (2.24)$$

the dephasing time is seen to be,

$$T_\varphi^\lambda = \frac{1}{\sqrt{2A_\lambda^2 (\partial_\lambda \omega_q)^2 |\ln(\omega_{ir} t)| + 2A_\lambda^4 (\partial_\lambda^2 \omega_q)^2 \ln^2(\omega_{ir} t)}}. \quad (2.25)$$

This pure dephasing time is estimated with $1/f$ noise. This is the noise source we will use in later chapters, but one could derive it using other power spectral functions. A lower bound frequency ω_{ir} is introduced and makes sure that the integral does not diverge. This lower bound is in literature [13, 17] assumed to be 2π Hz. The t is a characteristic time of the quantum system, we will use the same conservative value as ref. [17], $t = 1$ μs. The pure dephasing depends on how the qubit frequency depends on the external parameter. The spectrum computed from an external source, therefore, tells us how well the qubit is protected from pure dephasing. To get a better dephasing time one should engineer or tune a qubit to have sweet spots in the noisy parameters. Minimizing the slope and curvature of the spectrum due to the external parameter λ will give a better dephasing time. It is called sweet spots when the parameters are tuned such that the slope of the spectrum is 0.

Depolarization time

Bit flips that happen in a characteristic time are associated with a relaxation or excitation. We will ignore excitations as we work in the low temperature limit. This time is called the depolarization time. In this section, we start with the second term of Equation (2.7), which is the transverse terms in order to find the depolarization rate. The time-dependent Schrödinger equation is written where we now ignore the longitudinal terms,

$$i \frac{\mathrm{d}}{\mathrm{d}t} c_n(t) = \sum_{n', m \neq m'} v_{m,m'}(t) \langle n|m \rangle \langle m'|n' \rangle c_{n'}(t) = \sum_{n' \neq n} v_{n,n'}(t) c_{n'}(t). \quad (2.26)$$

We find the depolarization rate where the state starts in the first excited state and relaxes down to the ground state because it is only a two level system, $n = 0$ and $n' = 1$. Solving the differential equation and using Equation (2.7) to insert $v_{n,n'}$,

$$c_0(t) = -i \int_0^t \mathrm{d}t' \ \langle 0| \bar{V_\lambda}(t') |1\rangle = -i \int_0^t \mathrm{d}t' \ \langle 0| \mathrm{e}^{iH_0 t'} V_\lambda(t') \mathrm{e}^{-iH_0 t'} |1\rangle$$
$$= -i \int_0^t \mathrm{d}t' \ \langle 0| V_\lambda(t') |1\rangle \mathrm{e}^{-i\omega_q t'} = -i \langle 0| \partial_\lambda \mathcal{H} |1\rangle \int_0^t \mathrm{d}t' \, \delta\lambda(t') \mathrm{e}^{-i\omega_q t'}, \quad (2.27)$$

where $\omega_q = E_1 - E_0$. We have only gone to the first order in $\delta\lambda$ here. In order to find the transition rate from the excited to the ground state, we take the time derivative of the ensemble average of the absolute square of $c_0(t)$,

$$\left\langle |c_0(t)|^2 \right\rangle = |\langle 0| \partial_\lambda \mathcal{H} |1\rangle|^2 \int_0^t \mathrm{d}t_1 \int_0^t \mathrm{d}t_2 \ \langle \delta\lambda(t_2 - t_1)\delta\lambda(0)\rangle \mathrm{e}^{-i\omega_q(t_2 - t_1)}$$
$$= |\langle 0| \partial_\lambda \mathcal{H} |1\rangle|^2 S_\lambda(|\omega_q|)t, \quad (2.28)$$

the transition rate is then,

$$\Gamma_1^\lambda = \frac{\mathrm{d}}{\mathrm{d}t} \left\langle |c_0(t)|^2 \right\rangle = |\langle 0| \partial_\lambda \mathcal{H} |1\rangle|^2 S_\lambda(|\omega_q|). \quad (2.29)$$

This is also Fermi's golden rule for energy decay between $|1\rangle$ and $|0\rangle$. The depolarization time is then,

$$T_1^\lambda = \frac{1}{\Gamma_1^\lambda}. \quad (2.30)$$

We see the depolarization time depends on the overlap between the wave functions. By separating the wave functions the overlap will become less significant, and hence the depolarization time longer.

Chapter 3

Cicuit Quantum Electrodynamics (circuitQED)

From circuit to Hamiltonian

In this chapter, we will discuss how to go from a simple lumped circuit to a Hamiltonian. We need the Hamiltonian in order for us to analyze the energy eigenvalues and wave functions of the system we wish to make into a qubit. We know from classical electrodynamics how to draw simple schematics of circuits. Using Maxwell's equations together with Kirchhoff's laws the classical physics of such systems can be described. To determine the quantum mechanical effects at low temperatures, circuit quantum electrodynamics (circuitQED) can be used.

In circuits, we have nodes referred to as islands and branches between nodes. Each branch has a voltage difference $V_b(q_b)$ due to the charge difference between islands and a current $I_b(\Phi_b)$ flowing in the branch. Φ_b is the phase or flux and q_b is the charge on a branch between nodes. We can use classical electrodynamics to calculate the energy from either voltage difference between islands or currents flowing in branches [18, 19],

$$h(q_b) = \int_0^{q_b} \mathrm{d}q_b' \, V_b(q_b'), \qquad h(\Phi_b) = \int_0^{\Phi_b} \mathrm{d}\Phi_b' \, I_b(\Phi_b'), \qquad \dot{\Phi}_b(q_b) = V_b(q_b), \tag{3.1}$$

where it is noted that the change in the flux relates to a voltage drop. We define a reduced flux, $\phi_b = \frac{2\pi\Phi_b}{\Phi_0}$, which also will be referred to as the phase of a node, where $\Phi_0 = \frac{h}{2e}$ is the superconducting magnetic flux quantum.

The elements used most often in electrical circuits are capacitors, inductors, and resistors. We will assume that the superconducting circuits are with no resistance in the wires. Introducing the Josephson junction, a nonlinear component is

made available. A Josephson junction is formed when Cooper pairs are allowed to tunnel between two superconductors [20]. Components are placed between nodes on branches setting up circuit diagrams. Capacitative components have a voltage drop associated while inductive components have a current associated. From this, an energy can be calculated for each component,

$$V_b = \frac{q_b}{C_b}, \qquad h_C = \left(\frac{\Phi_0}{2\pi}\right)^2 \frac{C_b}{2}\dot{\phi}_b^2, \tag{3.2}$$

$$I_b = \frac{\Phi_0}{2\pi}\frac{\phi_b}{L_b}, \qquad h_L = \left(\frac{\Phi_0}{2\pi}\right)^2 \frac{\phi_b^2}{2L_b}, \tag{3.3}$$

$$I_b = I_0 \sin(\phi_b), \qquad h_{JJ} = -E_J \cos(\phi_b). \tag{3.4}$$

Everything until now is still classical electrodynamics, and the coordinates satisfy the Poisson bracket,

$$\begin{aligned} \{f, g\} &= \frac{\delta f}{\delta \Phi}\frac{\delta g}{\delta q} - \frac{\delta g}{\delta \Phi}\frac{\delta f}{\delta q}, \\ \{\Phi, q\} &= \frac{\delta \Phi}{\delta \Phi}\frac{\delta q}{\delta q} - \frac{\delta q}{\delta \Phi}\frac{\delta \Phi}{\delta q} = 1 - 0 = 1, \end{aligned} \tag{3.5}$$

whereas the quantum operators satisfy the commutation relation [15],

$$[\hat{\Phi}, \hat{q}] = \hat{\Phi}\hat{q} - \hat{q}\hat{\Phi} = i\hbar, \tag{3.6}$$

where operators are denoted by hats. For simplicity hats on operators are omitted from now on.

Like the reduced flux, we can define the reduced charge, $n = \frac{q}{2e}$, where n is the number operator, that counts the number of Cooper pairs on an island. ϕ and n then satisfy the commutation relation,

$$[\phi, n] = \frac{2\pi}{\Phi_0}\frac{1}{2e}[\Phi, q] = \frac{2\pi}{h}\hbar i = i, \tag{3.7}$$

meaning we can relate ϕ and n the same way as momentum and positions operators. A Lagrangian can then be constructed in phase space. The capacitative terms in energy correspond to the kinetic energy and inductive terms are potential terms,

$$\mathcal{L} = \sum_i (h_{Ci} - h_{Li} - h_{JJi}), \tag{3.8}$$

from this, the conjugate variables can be computed and by a Legendre transformation the Hamiltonian can be written [15, 18, 19],

$$
\begin{aligned}
q_i &= \frac{\partial \mathcal{L}}{\partial \dot{\Phi}_i} = \frac{2e}{\hbar}\frac{\partial \mathcal{L}}{\partial \dot{\phi}_i}, \\
\mathcal{H} &= \sum_i \dot{\Phi}_i q_i - \mathcal{L} = \frac{\hbar}{2e}\sum_i \dot{\phi}_i q_i - \mathcal{L}.
\end{aligned} \tag{3.9}
$$

From Harmonic LC-oscillator to Anharmonic Transmon

The simplest superconducting circuit is the LC-oscillator (Figure 3.1a) consisting of an inductor and capacitor in parallel. Constructing the Lagrangian following the above and finding the conjugate variable,

$$
\begin{aligned}
\mathcal{L} &= \left(\frac{\Phi_0}{2\pi}\right)^2 \frac{C}{2}\dot{\phi}^2 - \left(\frac{\Phi_0}{2\pi}\right)^2 \frac{\phi^2}{2L}, \\
q &= \frac{2e}{\hbar}\frac{\partial \mathcal{L}}{\partial \dot{\phi}} = \frac{\hbar}{2e} C\dot{\phi},
\end{aligned} \tag{3.10}
$$

doing the Legendre transformation we arrive at the Hamiltonian,

$$
\mathcal{H} = \frac{q^2}{2C} + \left(\frac{\Phi_0}{2\pi}\right)^2 \frac{\phi^2}{2L}. \tag{3.11}
$$

We associate the charge as the momentum and the phase as the position of the system. Each term can be associated with an energy. The first term is the kinetic energy and the second is the potential energy. The capacitance, C, can be associated with the mass of the mode of the branch it is on. By increasing or decreasing the capacitance we make the system heavier or lighter. Heavy systems are localized in phase space and spread out in charge space and vice versa. Superconducting circuits are often seen as artificial atoms. CircuitQED is adapted and closely related to cavityQED from quantum optics. CavityQED analyzes real atoms in cavities. Writing the charge in terms of Cooper pairs $q = 2e(n - n_g)$ and the capacitance in terms of the charging energy $E_C = \frac{e^2}{2C}$ the Hamiltonian is,

$$
\mathcal{H} = 4E_C(n - n_g)^2 + \frac{\phi^2}{2L}, \tag{3.12}
$$

where n_g is an offset charge. An offset charge can be achieved by changing the number of Cooper pairs on an island. The Hamiltonian in Equation (3.12) is a

quantum harmonic oscillator with equal spacing between energy levels. Due to that, the LC-oscillator is not a good candidate for a qubit, as it is not possible to make a subspace of only two states.

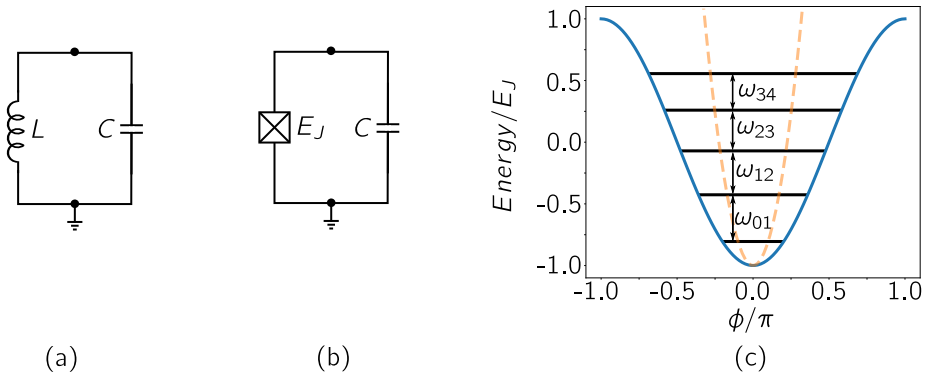

Figure 3.1: (a) Circuit of LC-oscillator. (b) Circuit of Cooper Pair box or Transmon. (c) Potential of quantized (dashed orange line) LC-oscillator and (solid blue line) Transmon. Solid black lines are eigenenergies of Transmon with $n_g = 0$ and $E_J/E_C = 50$. The eigenenergies are anharmonic meaning it is possible to operate in a qubit subspace, unlike the harmonic LC-oscillator where it is impossible.

The Cooper pair box (Figure 3.1b) [21] was the first qubit to use the nonlinear Josephson junction to make an anharmonic oscillator, but the dephasing due to charge noise was not optimal. The Transmon [11] is built from the same circuit as the Cooper pair box (Figure 3.1b), but is a capacitively shunted with a larger capacitor. The Transmon has an increased dephasing time and is one of the most used superconducting qubits due to the large anharmonicity of the spectrum which is shown in Figure 3.1c. The anharmonicity is defined as $a \equiv \omega_{12} - \omega_{01}$ where $\omega_{01} = \omega_q$.
The Lagrangian is found to be,

$$\mathcal{L} = \left(\frac{\Phi_0}{2\pi}\right)^2 \frac{C}{2}\dot{\phi}^2 + E_J \cos\phi, \tag{3.13}$$

Doing the Legendre transformation and rewriting in terms of Cooper pairs and charging energy,

$$\mathcal{H} = 4E_C(n - n_g)^2 - E_J \cos\phi, \tag{3.14}$$

where n_g is a charge offset.

In Figure 3.2 the Hamiltonian for the Transmon in Equation (3.14) is solved numerically and the spectrum as a function of charge offset is obtained. By changing the ratio E_J/E_C, the mass of the system is effectively changed. By increasing the capacitance in the Transmon the charging energy is lowered, which is analog to increasing the mass of the mode. When the mode gets heavier we see that the energy bands get flatter, meaning the derivative of the qubit frequency decreases, and thereby a good dephasing time is acquired. There is not much to be done about the depolarization time as there is always an overlap between the wave functions of the qubit. A way to make wave functions with small overlap could be by separating them in a double well potential and having degenerate qubit eigenstates.

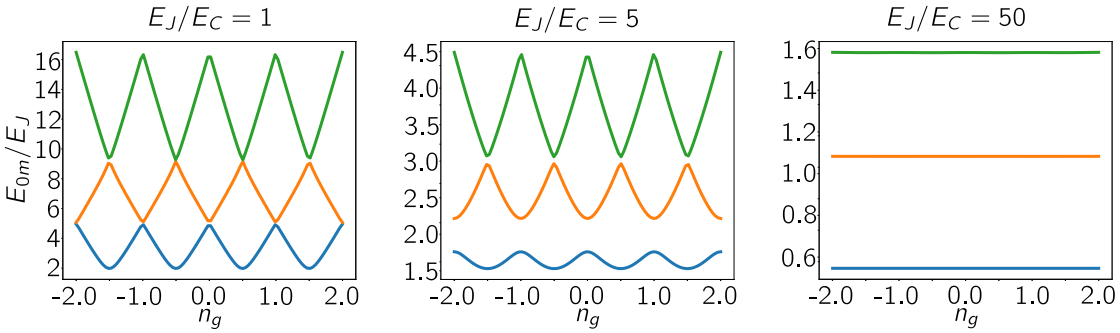

Figure 3.2: Energy levels E_{0m} for the first three levels $m = 1, 2, 3$ with varing charge offset. Figure inspired from [11].

Numerical analysis of Hamiltonian

To simulate the continuous Hamiltonian we derive for a given circuit, a discrete matrix representation is needed. The implementation is different depending on the chosen basis. It is often chosen to work in either charge basis or flux basis. In this section, we will go through the matrix representation in each basis and how to construct a Hamiltonian. This section is inspired from [22].

Charge Basis

In charge basis, a finite grid is defined for the charge. A diagonal matrix is then representing the number of cooper pairs on an island. Here the matrix is:

$$n = \begin{pmatrix} -n_{cutoff} & & & & \\ & -n_{cutoff}+1 & & & \\ & & \ddots & & \\ & & & n_{cutoff}-1 & \\ & & & & n_{cutoff} \end{pmatrix}. \tag{3.15}$$

Designing circuits without any linear inductors means that the phase only appears in cosine terms. We can rewrite cosine in terms of exponential functions,

$$\cos(\phi) = \frac{1}{2}\left(\mathrm{e}^{i\phi} + \mathrm{e}^{-i\phi}\right), \tag{3.16}$$

these terms are describing a jump of cooper pairs in the Josephson junctions. The jump operator in the charge basis is represented by:

$$\mathrm{e}^{i\phi} = \left(\mathrm{e}^{-i\phi}\right)^{\dagger} = \begin{pmatrix} 0 & & & \\ 1 & 0 & & \\ & \ddots & \ddots & \\ & & 1 & 0 \end{pmatrix}. \tag{3.17}$$

If more phase modes are present in a cosine, or a bias flux is passing through a loop in the circuit we can write it as,

$$\cos\left(\phi_1 - \phi_2 + \phi_{ext}\right) = \frac{1}{2}\left(\mathrm{e}^{i\phi_{ext}}\left(\mathrm{e}^{i\phi_1} \otimes \mathrm{e}^{-i\phi_2}\right) + \mathrm{e}^{-i\phi_{ext}}\left(\mathrm{e}^{-i\phi_1} \otimes \mathrm{e}^{i\phi_2}\right)\right). \tag{3.18}$$

Flux Basis

In flux basis the phase operator is a diagonal matrix,

$$\phi = \begin{pmatrix} -\phi_{max} & & & & \\ & -\phi_{max}+\delta\phi & & & \\ & & \ddots & & \\ & & & \phi_{max}-\delta\phi & \\ & & & & \phi_{max} \end{pmatrix}, \tag{3.19}$$

where we use 2π-periodic boundary conditions, $\phi_{max} = \pi$, then the grid goes from $-\pi$ to π. $\delta\phi$ defines how fine the resolution we simulate is. The phase is

a continuous variable, $\delta\phi$ determines how good the approximation is, however the matrix size and computation time depend on the choice of $\delta\phi$. The canonical conjugate operator n is the partial derivative, $n = -i\partial_\phi$. To represent the derivate as a hermitian matrix we use the finite difference method,

$$n = \frac{-i}{2\delta\phi}\begin{pmatrix} 0 & 1 & & & \\ -1 & 0 & 1 & & \\ & \ddots & & & \\ & & -1 & 0 & 1 \\ & & & -1 & 0 \end{pmatrix}. \tag{3.20}$$

In both bases, we can have more modes for a system. To combine them we have to use the tensor product. If we have two modes then the phase operator for the first and second mode is given by,

$$\phi_1 = \phi \otimes \mathbb{1}, \quad \phi_2 = \mathbb{1} \otimes \phi, \tag{3.21}$$

and similar for other operators. The two bases will yield the same result, but one can be easier to implement than the other for different problems. Now the problem can be solved numerically by finding eigenvalues and eigenvectors. In our case, we use the numpy and scipy packages in Python.

Chapter 4

Encoding of Flensmon

In the previous chapter, we covered the Cooper pair box and the Transmon. These are charge qubits, where the charge is a good quantum number. The Transmon had a flat spectrum due to charge noise, but one cannot engineer a better depolarization time, as the wave functions are not delocalized. Instead of having charge as the good quantum number, a superconducting ring could be formed where a magnetic flux threads through the loop. The magnetic flux that is passed through the ring generates a persistent current. This is a flux qubit and the first generation was called the persistent-current flux qubit [12]. Only an integer number of flux quanta are allowed and therefore the current will only flow clockwise or counter-clockwise [23]. The flux is then a good quantum number in flux qubits.

Another qubit could be a topologically protected qubit that exploits the nature of non-Abelian anyons [24]. Topological protected qubits have been theoretically proposed, e.g. to find the Majorana zero modes in a Kitaev chain liking nanowire [25]. However, this has not yet been realized experimentally.

When developing new qubits one has to think about the coherence times, the matrix elements in the qubit subspace, and how the spectrum looks. Besides having qubits with long lifetimes, one needs to make operations on them, therefor both single and two qubit gates are essential, the latter to make it scalable. Finally, we need to be able to collapse and readout which state the qubit is in.

To engineer a protected qubit we need to think of the overlap between the qubit levels to make a good depolarization time, T_1, and make the spectrum flat in the external parameters which disturb or control the qubit. A good theoretical prediction of a protected qubit by Brooks, Kitaev, and Preskill is the $0-\pi$ qubit [26], this qubit is predicted to have very long coherence times. In practice, it has been hard to build large superinductors and symmetric design [27]. We aspire to develop a qubit that is decently protected, while easy to construct and operate in

the laboratory.

This chapter focuses on the circuit of the Flensmon qubit, which is named after Karsten Flensberg. We will compute the spectrum and estimate coherence times in the parameter regime we have chosen.

Circuit QED of the Flensmon

The Flensmon is derived from the superconducting persistent-current qubit [12], which was the first flux qubit suggested. This never got a breakthrough, but it was later revisited, as the capacitively shunted flux qubit (CSFQ) [13]. Now we will revisit the same circuit topology but in a different parameter regime.

The circuit consists of a loop with three islands with three Josephson junctions, each in parallel with a capacitor. The circuit is depicted in Figure 4.1. This setup has two degrees of freedom. We will write the Hamiltonian as in Chapter 3.

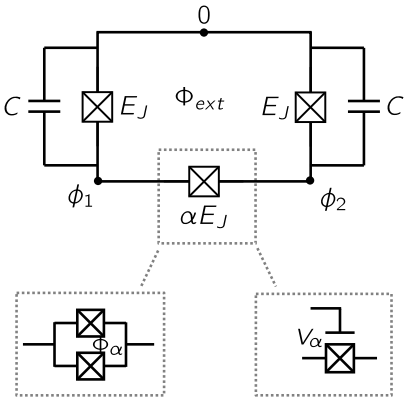

Figure 4.1: Circuit of the Flensmon we simulate in this thesis. There are three islands with a Josephson junction between each. Two of the junctions are capacitively shunted. The third junction is a tunable junction. It can either be tuned by making a superconducting quantum interference device (SQUID), or using a gate tunable junction. The circuit has two modes.

Each Josephson junction has a Josephson capacitance defined by the area between the superconductors. The total capacitances are given by,

$$C_1 = C_{01} + C_J, \quad C_2 = C_{02} + C_J, \quad C_3 = C_{12} + C_J, \tag{4.1}$$

where C_J is the Josephson capacitance of a junction, C_{ij} is the capacitance between island i and j, in Figure 4.1 $C_{12} = 0$. Often the Josephson capacitance is

omitted for simplicity because it is many orders of magnitude smaller than the shunting capacitors. We can write up the Lagrangian for the circuit,

$$\mathcal{L} = \left(\frac{\Phi_0}{2\pi}\right)^2 \left(\frac{C_1}{2}\dot{\phi_1}^2 + \frac{C_2}{2}\dot{\phi_2}^2 + \frac{C_3}{2}\left(\dot{\phi_1} - \dot{\phi_2}\right)^2\right) + E_{J1}\cos(\phi_1) + E_{J2}\cos(\phi_2) + E_{J3}\cos(\phi_1 - \phi_2 + \Phi_{ext}). \tag{4.2}$$

With the Lagrangian, we compute the conjugate variables to the superconducting phase,

$$q_1 = \frac{2e}{\hbar}\frac{\partial \mathcal{L}}{\partial \dot{\phi_1}} = \frac{\hbar}{2e}\Big(C_1\dot{\phi_1} + C_3\left(\dot{\phi_1} - \dot{\phi_2}\right)\Big), \tag{4.3}$$

$$q_2 = \frac{2e}{\hbar}\frac{\partial \mathcal{L}}{\partial \dot{\phi_2}} = \frac{\hbar}{2e}\Big(C_2\dot{\phi_2} + C_3\left(\dot{\phi_2} - \dot{\phi_1}\right)\Big), \tag{4.4}$$

solving for $\dot{\phi_1}$ and $\dot{\phi_2}$ we arrive at

$$\dot{\phi_1} = \frac{2e}{\hbar}\left(\frac{C_2q_1 + C_3q_1 + C_3q_2}{C_1C_2 + C_1C_3 + C_2C_3}\right) = \frac{2e}{\hbar}\left(\frac{C_2q_1 + C_3q_1 + C_3q_2}{C_\Sigma^2}\right), \tag{4.5}$$

$$\dot{\phi_2} = \frac{2e}{\hbar}\left(\frac{C_3q_1 + C_1q_2 + C_3q_2}{C_1C_2 + C_1C_3 + C_2C_3}\right) = \frac{2e}{\hbar}\left(\frac{C_3q_1 + C_1q_2 + C_3q_2}{C_\Sigma^2}\right), \tag{4.6}$$

where $C_\Sigma^2 = C_1C_2 + C_1C_3 + C_2C_3$. The Hamiltonian can now be written as,

$$\mathcal{H} = \frac{\hbar}{2e}\Big(\dot{\phi_1}q_1 + \dot{\phi_2}q_2\Big) - \mathcal{L}, \tag{4.7}$$

$$= \frac{\hbar}{2e}\Big(\dot{\phi_1}q_1 + \dot{\phi_2}q_2\Big) - \left(\frac{C_1}{2}\dot{\phi_1}^2 + \frac{C_2}{2}\dot{\phi_2}^2 + \frac{C_3}{2}\left(\dot{\phi_1} - \dot{\phi_2}\right)^2\right) - \left(E_{J1}\cos(\phi_1) + E_{J2}\cos(\phi_2) + E_{J3}\cos(\phi_1 - \phi_2 + \Phi_{ext})\right), \tag{4.8}$$

in which we substitute $\dot{\phi_1}$ and $\dot{\phi_2}$. We look at the first two terms separately,

$$\frac{\hbar}{2e}\Big(\dot{\phi_1}q_1 + \dot{\phi_2}q_2\Big) = \frac{C_3q_1^2 + C_2q_1^2 + C_1q_2^2 + C_3q_2^2 + 2C_3q_1q_2}{C_\Sigma^2}, \tag{4.9}$$

and the second term can be rewritten to the same form,

$$\frac{C_1}{2}\dot{\phi_1}^2 + \frac{C_2}{2}\dot{\phi_2}^2 + \frac{C_3}{2}\left(\dot{\phi_1} - \dot{\phi_2}\right)^2 \tag{4.10}$$

$$= \frac{1}{2C_\Sigma^4}\Big(C_1C_2\left(C_3q_1^2 + C_2q_1^2 + C_1q_2^2 + C_3q_2^2 + 2C_3q_1q_2\right)$$
$$+ C_1C_3\left(C_3q_1^2 + C_2q_1^2 + C_1q_2^2 + C_3q_2^2 + 2C_3q_1q_2\right)$$
$$+ C_2C_3\left(C_3q_1^2 + C_2q_1^2 + C_1q_2^2 + C_3q_2^2 + 2C_3q_1q_2\right)\Big) \tag{4.11}$$

$$= \frac{C_3q_1^2 + C_2q_1^2 + C_1q_2^2 + C_3q_2^2 + 2C_3q_1q_2}{2C_\Sigma^2} \tag{4.12}$$

we arrive at the Hamiltonian,

$$\mathcal{H} = \frac{C_2q_1^2 + C_1q_2^2 + C_3\left(q_1 + q_2\right)^2}{2C_\Sigma^2}$$
$$- E_{J1}\cos(\phi_1) - E_{J2}\cos(\phi_2) - E_{J3}\cos(\phi_1 - \phi_2 + \Phi_{ext}), \tag{4.13}$$

where the first terms refer to the charging energy $\mathcal{T}$ and the rest is the potential energy $\mathcal{V}$. The charge $q_i = 2en_i$ corresponding to the number of Cooper pairs on an island. We define the charging energy of an island, $E_{Ci} = \frac{e^2}{2C_i} \Leftrightarrow C_i = \frac{e^2}{2E_{C_i}}$. We first rewrite C_Σ^2,

$$C_\Sigma^2 = C_1C_2 + C_1C_3 + C_2C_3 = \frac{e^4}{4}\left(\frac{1}{E_{C1}E_{C2}} + \frac{1}{E_{C1}E_{C3}} + \frac{1}{E_{C2}E_{C3}}\right) \equiv \frac{e^4}{4}\frac{1}{E_\Sigma^2}, \tag{4.14}$$

meaning that the kinetic energy term is,

$$\mathcal{T} = \frac{4E_\Sigma^2}{e^4}\frac{4e^2\left(\frac{e^2}{2E_{C2}}n_1^2 + \frac{e^2}{2E_{C1}}n_2^2 + \frac{e^2}{2E_{C3}}\left(n_1 + n_2\right)^2\right)}{2} \tag{4.15}$$

$$= 4E_\Sigma^2\left(\frac{n_1^2}{E_{C2}} + \frac{n_2^2}{E_{C1}} + \frac{\left(n_1 + n_2\right)^2}{E_{C3}}\right). \tag{4.16}$$

Finally, the Hamiltonian is,

$$\mathcal{H} = 4E_\Sigma^2\left(\frac{n_1^2}{E_{C2}} + \frac{n_2^2}{E_{C1}} + \frac{\left(n_1 + n_2\right)^2}{E_{C3}}\right)$$
$$- E_{J1}\cos(\phi_1) - E_{J2}\cos(\phi_2) - E_{J3}\cos(\phi_1 - \phi_2 + \phi_{ext}). \tag{4.17}$$

This Hamiltonian has the same form as both the flux qubit by Orlando et al. [12] and the CSFQ by Yan et al. [13]. The flux qubit operates in a regime where all modes are light, e.g. small capacitors and two of the junctions are of equal size and the last is tuned to $E_{J3} = 0.8E_J$. CSFQ uses two large capacitors over junctions E_{J1} and E_{J2}. The last junction is tuned to $E_{J3} = 0.5E_J$. This makes one large well where the eigenfunctions live in. This means that they do not have delocalized states, but the spectrum with respect to the external flux is not linear [13]. The Hamiltonian has two modes, and we will refer to them as the ϕ and θ modes. They are defined as,

$$\begin{aligned} 2\phi &= \phi_1 - \phi_2, \\ 2\theta &= \phi_1 + \phi_2. \end{aligned} \tag{4.18}$$

The potential has a double well in the ϕ direction, where α determines the barrier between the two wells. For $\alpha = 0.5$ in the CSFQ regime the potential is just a single well. The potential in one dimension is shown in Figure 4.2 with the first few energies. We see the anharmonicity is good in this qubit, but as there is only one well, the wave functions will not be delocalized. The anharmonicity is defined as $a = \omega_{12} - \omega_{01}$. Note the second and third excited states are almost degenerate.

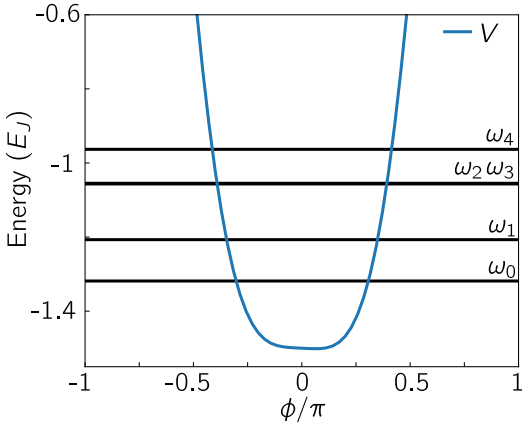

Figure 4.2: Potential in the ϕ direction with CSFQ parameters. $\alpha = 0.5$ and $E_J/E_C = 100$. Blue line is the potential, black lines are the energies spanning from the ground state to the forth excited state. The second and third excited states are almost degenerate. The flux through the loop is $\phi_{ext} = 0.997\pi$.

The Flensmon is in a parameter regime between the persistent-current qubit and the CSFQ. We wish to shunt the qubit like in the CSFQ, but also have a double well like the persistent-current qubit. We will use $C_1 = C_2 = C$ and $C_3 = 0$

like sketched in Figure 4.1. The Josephson capacitance in the tunable junction is ignored. The Josephson energies will be of equal size, where the third junction is a tunable junction, $E_{J1} = E_{J2} = E_J$ and $E_{J3} = \alpha E_J$. There are several methods for tuning a junction, a superconducting quantum interference device (SQUID) is a well-known method. Here an external magnetic field shifts the energy of the effective junction. A gateable junction is also an opportunity where a semiconductor material is placed between the superconductors in the junction. This allows us with a gate voltage to define the tunneling energy of the junction and by that controlling the Josephson energy. The Hamiltonian for the Flensmon is,

$$\mathcal{H} = 4E_C\left((n_1 - n_{g1})^2 + (n_2 - n_{g2})^2\right) - E_J(\cos(\phi_1) + \cos(\phi_2) + \alpha\cos(\phi_1 - \phi_2 + \phi_{ext})). \tag{4.19}$$

Here we have added n_{g1} and n_{g2} which correspond to a charge offset on each island. This can be tuned by adding gate voltages to the islands.

To localize the two qubit states in the wells we need to make them heavy. This is done by increasing capacitances in the circuit and having high E_J/E_C. We will use $E_J/E_C = 100$. The two-dimensional potential and a one-dimensional line cut with the two lowest eigenstates are shown in Figure 4.3. The unit cell of the potential is $-\pi < \phi_1, \phi_2 < \pi$, and is periodic.

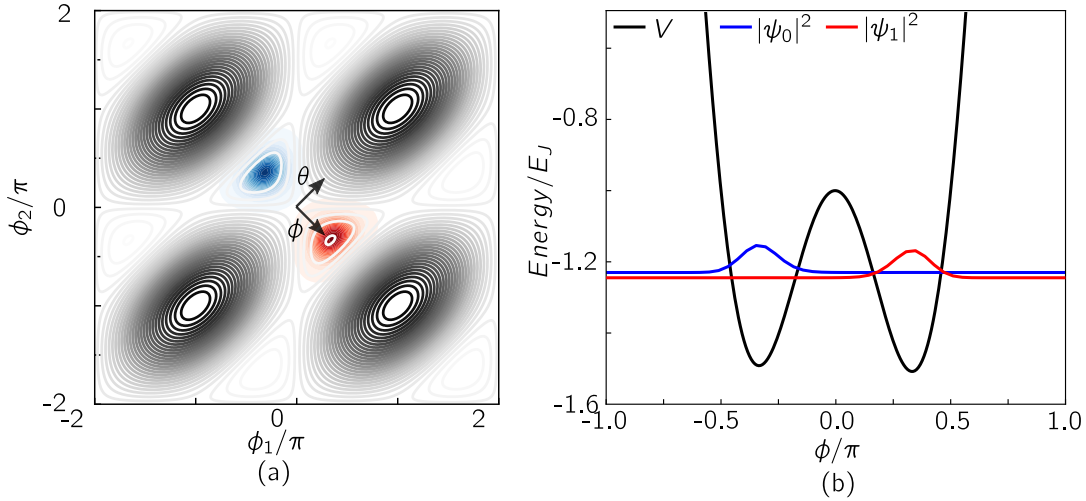

Figure 4.3: (a) Potential landscape of the Flensmon with $E_J/E_C = 100$ and $\alpha = 1$. The basis change to $2\phi = \phi_1 - \phi_2$ and $2\theta = \phi_1 + \phi_2$ is indicated. (b) One-dimensional cut of the ϕ mode, with the two qubit states shown. In both figures the external magnetic field is $\Phi_{ext} = 0.997\pi$, in order not to be in an artificial sweetspot.

The qubit subspace is localized in each of the two wells. We can see on Figure 4.3b that the overlap between the two wave functions is exponentially small, which will give a good depolarization time, T_1. We have determined the ground state, as we do not have precisely half flux quantum through the loop, this causes one of the wells to be slightly deeper than the other one. We are slightly away from half flux quantum, as it is impossible in an experiment to thread a flux through the loop, at precisely $\Phi_{ext} = \frac{\Phi_0}{2}$. The two states correspond to the current running either clockwise or counter-clockwise in the loop. Charge offsets in the Hamiltonian are tuned with a gate voltage on the islands. If we are heavy enough, the spectrum as a function of a charge offset would be flat. Other parameters which we can tune are the flux through the loop or the Josephson energy of the tunable junction.

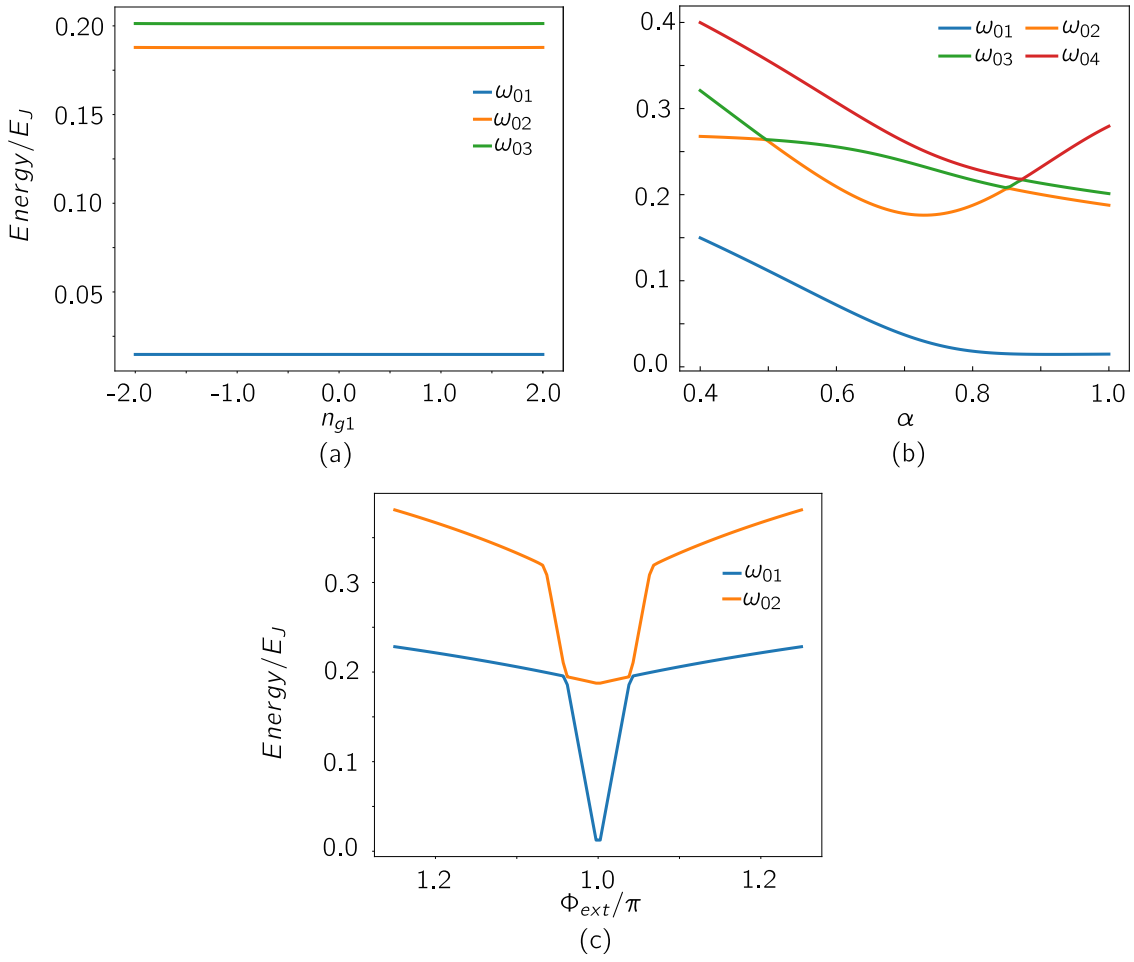

Figure 4.4: Spectrum of the different external parameters. (a) Varying the charge offset over junction 1. (b) Varying the tunable junction. (c) Varying the external magnetic field through the loop.

The spectrums of the three different external variables are shown in Figure 4.4.

We see that the spectrum is flat as a function of charge offset in Figure 4.4a. The spectrum is also flat as a function of the tunable junction between $\alpha = 0.8$ and $\alpha = 1$ in Figure 4.4b. We are mostly interested in the blue curves as these are our computational subspace to make the qubit. The dispersion is linear when changing the external magnetic field (Figure 4.4c). This means the dephasing time will be bad if there are fluctuations in the field through the loop. In the next section, we will look at the decoherence for the Flensmon qubit. There is a sweet spot for the external flux when $\phi_{ext} = \pi$, though it can be hard experimentally to be fixed at this point.

Decoherence of Flensmon

In this thesis, we concentrate on three different noise channels. We look at the external flux, fluctuations in charge offset, and the noise of the critical current of a junction. We will use the derived formulas from Chapter 2 and show the equations we use for each noise parameter. When finding depolarization times we use the derivative of the Hamiltonian from Equation (4.19) with respect to the external noise parameter. The pure-dephasing time is found by solving the same Hamiltonian numerically and using the first and second derivative of the qubit frequency with respect to the external noise parameter. We can already look at the spectrums in Figure 4.4 to get an idea what of noise source is the dominant source of the dephasing time. The relevant equations are,

$$\Gamma_1^\lambda = \left| \langle 1 | \frac{\partial \mathcal{H}}{\partial \lambda} | 0 \rangle \right|^2 S_\lambda(|\omega_q|) \tag{4.20}$$

$$T_\varphi^\lambda = \frac{1}{\sqrt{2A_\lambda^2(\partial_\lambda \omega_q)^2(\ln(\omega_{ir}t)) + 2A_\lambda^4(\partial_\lambda^2 \omega_q)^2 \ln^2(\omega_{ir}t)}}, \tag{4.21}$$

we use $1/f$ noise, the noise power spectrum is then $S_\lambda(|\omega_q|) = \frac{2\pi A_\lambda^2}{|\omega_q|}$, where A_λ is the noise amplitude.

Noise in external flux

We look at the depolarization due to global flux noise, Φ_{ext}. It is believed that the fluctuations of surface spins in superconducting circuits give rise to a $1/f$ flux noise [28]. The external reduced flux is given by $\phi_{ext} = \frac{2\pi\Phi_{ext}}{\Phi_0}$, where Φ_0 is the flux quantum. We first find the derivative of the Hamiltonian,

$$\frac{\partial \mathcal{H}}{\partial \Phi_{ext}} = \frac{\partial \mathcal{H}}{\partial \phi_{ext}} \frac{\partial \phi_{ext}}{\partial \Phi_{ext}} = \frac{2\pi}{\Phi_0} \frac{\partial \mathcal{H}}{\partial \phi_{ext}} = \frac{2\pi}{\Phi_0} E_{J3} \sin(\phi_1 - \phi_2 + \phi_{ext}). \tag{4.22}$$

We put this into Equation (4.20) and use $1/f$ noise power spectrum and $E_{J3} = \alpha E_J$.

$$\begin{aligned} \Gamma_1^{\Phi_{ext}}/E_J &= |\langle 1| \sin(\phi_1 - \phi_2 + \phi_{ext}) |0\rangle|^2 \frac{(2\pi)^2}{\Phi_0^2} \frac{2\pi A_{\Phi ext}^2}{|\omega_q|} \alpha^2 E_J \\ &= |\langle 1| \sin(\phi_1 - \phi_2 + \phi_{ext}) |0\rangle|^2 (2\pi)^3 \frac{A_{\Phi_{ext}}^2 \alpha^2}{\Phi_0^2 |\omega_q|} E_J. \end{aligned} \tag{4.23}$$

To find the depolarization time we just take the inverse of the transition rate and choose an energy of the Josephson junctions, E_J.
Pure-dephasing is similar. Here we need to look at the derivate of the qubit frequency with respect to the external flux.

$$\begin{aligned} \frac{\partial \omega_q}{\partial \Phi_{ext}} &= \frac{2\pi}{\Phi_0} \frac{\partial \omega_q}{\partial \phi_{ext}}, \\ \frac{\partial^2 \omega_q}{\partial \Phi_{ext}^2} &= \left(\frac{2\pi}{\Phi_0}\right)^2 \frac{\partial^2 \omega_q}{\partial \phi_{ext}^2}, \end{aligned} \tag{4.24}$$

this is put into Equation (4.21),

$$T_\varphi^{\Phi_{ext}} = \frac{1}{\sqrt{2\left(\frac{A_{\Phi_{ext}} 2\pi}{\Phi_0}\right)^2 (\partial_{\phi_{ext}} \omega_q)^2 (\ln(\omega_{ir} t)) + 2\left(\frac{A_{\Phi_{ext}} 2\pi}{\Phi_0}\right)^4 \left(\partial_{\phi_{ext}}^2 \omega_q\right)^2 \ln^2(\omega_{ir} t)}}. \tag{4.25}$$

The amplitude of the noise of the external flux used in simulations is $A_{\Phi_{ext}} = 10^{-6}\Phi_0$ [17].

Noise in charge offset

The decoherence due to fluctuations in charge offset is found by the same approach as the external flux. Fluctuations in charge offset are hard to control, as electrons from the environment easily can interfere with the total charge of an island. The Flensmon has a flat band due to charge offset, this indicates that the dephasing due to charge noise should not be the limiting factor. The derivatives are a little different. We define the charge as a Cooper pair, $q_{gi} = 2en_{gi}$ where i is the i'th island.

$$\frac{\partial \mathcal{H}}{\partial q_{g1}} = \frac{\partial \mathcal{H}}{\partial n_{g1}} \frac{\partial n_{g1}}{\partial q_{g1}} = \frac{1}{2e} \frac{\partial \mathcal{H}}{\partial n_{g1}} = \frac{-8E_C(n_1 - n_{g1})}{2e}, \tag{4.26}$$

the transistion rate is then,

$$\Gamma_1^{n_{g1}} = |\langle 1| (n_1 - n_{g1}) |0\rangle|^2 (8E_C)^2 \frac{2\pi \left(\frac{A_{n_g}}{2e}\right)^2}{|\omega_q|}. \tag{4.27}$$

Now we look at the derivative of the qubit frequency, in order to estimate the pure-dephasing time,

$$\begin{aligned} \frac{\partial \omega_q}{\partial q_{g1}} &= \frac{1}{2e} \frac{\partial \omega_q}{\partial n_{g1}}, \\ \frac{\partial^2 \omega_q}{\partial q_{g1}^2} &= \left(\frac{1}{2e}\right)^2 \frac{\partial^2 \omega_q}{\partial n_{g1}^2}, \end{aligned} \tag{4.28}$$

and the pure dephasing time is,

$$T_\varphi^{n_{g1}} = \frac{1}{\sqrt{2\left(\frac{A_{n_g}}{2e}\right)^2 \left(\partial_{n_{g1}} \omega_q\right)^2 (\ln(\omega_{ir} t)) + 2\left(\frac{A_{n_g}}{2e}\right)^4 \left(\partial_{n_{g1}}^2 \omega_q\right)^2 \ln^2(\omega_{ir} t)}}. \tag{4.29}$$

The amplitude of the noise due to charge fluctuations is $A_{n_g} = 10^{-4} e$ [17].

Noise from critical current in the tunable junction

The last noise source we look at is variations in the critical current in the tunable junction. The critical current is defined $I_{C3} = \frac{2\pi E_{J3}}{\Phi_0}$, and we remember $E_{J3} = \alpha E_J$. Low frequency noise due to the critical current in a Josephson junction, is believed to come from charge traps in the barrier of the tunnel junction [29], but the critical current noise is not fully understood yet. The derivate of the Hamiltonian is found as usual,

$$\frac{\partial \mathcal{H}}{\partial I_{C3}} = \frac{\partial \mathcal{H}}{\partial E_{J3}} \frac{\partial E_{J3}}{\partial I_{C3}} = \frac{\Phi_0}{2\pi} \frac{\partial \mathcal{H}}{\partial E_{J3}} = -\frac{\Phi_0}{2\pi} \cos(\phi_1 - \phi_2 + \phi_{ext}), \tag{4.30}$$

we put this into Fermi's Golden rule in order to estimate the transition rate which is used to find the depolarization time,

$$\Gamma_1^\alpha = |\cos(\phi_1 - \phi_2 + \phi_{ext})|^2 \left(\frac{\Phi_0}{2\pi}\right)^2 \frac{2\pi A_{I_{C3}}^2}{|\omega_q|}. \tag{4.31}$$

Next we calculate the slope and curvature of the qubit frequency due to the critical current in the third junction,

$$\begin{aligned} \frac{\partial \omega_q}{\partial I_{C3}} &= \frac{\Phi_0}{2\pi}\frac{\partial \omega_q}{\partial E_{J3}} = \frac{\Phi_0}{2\pi}\frac{\partial \alpha}{\partial E_{J3}}\frac{\partial \omega_q}{\partial \alpha} = \frac{\Phi_0}{2\pi E_J}\frac{\partial \omega_q}{\partial \alpha}, \\ \frac{\partial^2 \omega_q}{\partial I_{C3}^2} &= \left(\frac{\Phi_0}{2\pi E_J}\right)^2 \frac{\partial^2 \omega_q}{\partial \alpha^2}, \end{aligned} \tag{4.32}$$

finally, the dephasing time is found,

$$T_\varphi^\alpha = \frac{1}{\sqrt{2\left(\frac{A_{I_{C3}}\Phi_0}{2\pi E_J}\right)^2 (\partial_\alpha \omega_q)^2 (\ln(\omega_{ir} t)) + 2\left(\frac{A_{I_{C3}}\Phi_0}{2\pi E_J}\right)^4 (\partial_\alpha^2 \omega_q)^2 \ln^2(\omega_{ir} t)}}. \tag{4.33}$$

The amplitude of the noise due to critical current is $A_{I_{C3}} = 10^{-7} I_{C3} = 10^{-7} \frac{2\pi\alpha E_J}{\Phi_0}$ [17].

Simulations of coherence times

In the previous subsections, we have shown the relevant formulas for finding coherence times. All coherence times are calculated by solving the Hamiltonian in Equation (4.19) numerically. The overlap in the transition rate Γ_1 is found by taking the overlap with the matrix representation of the differentiated Hamiltonian with the eigenstates $|\psi_0\rangle$ and $|\psi_1\rangle$. The derivatives of the qubit frequencies are found by the finite difference method,

$$\begin{aligned} \partial_\lambda \omega_q &= \frac{\omega_q(\lambda + \Delta\lambda) - \omega_q(\lambda - \Delta\lambda)}{2\Delta\lambda}, \\ \partial_\lambda^2 \omega_q &= \frac{\omega_q(\lambda + \Delta\lambda) - 2\omega_q(\lambda) + \omega_q(\lambda - \Delta\lambda)}{\Delta\lambda^2}, \end{aligned} \tag{4.34}$$

where $\Delta\lambda$ is how much we change the external parameter. This gives a good idea of the slope and curvature of the spectrum due to a change in an external parameter. We investigate how the coherence times change when we tune α. The calculated coherence times are shown in Figure 4.5, where the depolarization times are shown in (a) and dephasing times are shown in (b). As expected, the dephasing due to flux noise is the limiting one, as the spectrum is linear in Figure 4.4c.

We see that when one approaches the limit of the CSFQ regime, the dephasing time gets better, but as shown earlier, this is no longer a double well potential. Note that when α is lowered the qubit states become less degenerate. For low α the $1/f$ power spectrum might not be the right to consider anymore, but rather the ohmic power spectrum could be considered. This has not been done in this thesis. In the next chapter, we will look into how we can improve the dephasing time due to global flux noise. This is a known problem with a flux qubit with three Josephson junctions of the same size, and because of that we often see α tuned to a slightly smaller value, to have a better dephasing time, but this causes a worse depolarization time. For all simulations we have picked $E_J/E_C = 100$ and $E_J = 10\,h$GHz, where h is Planck's constant.

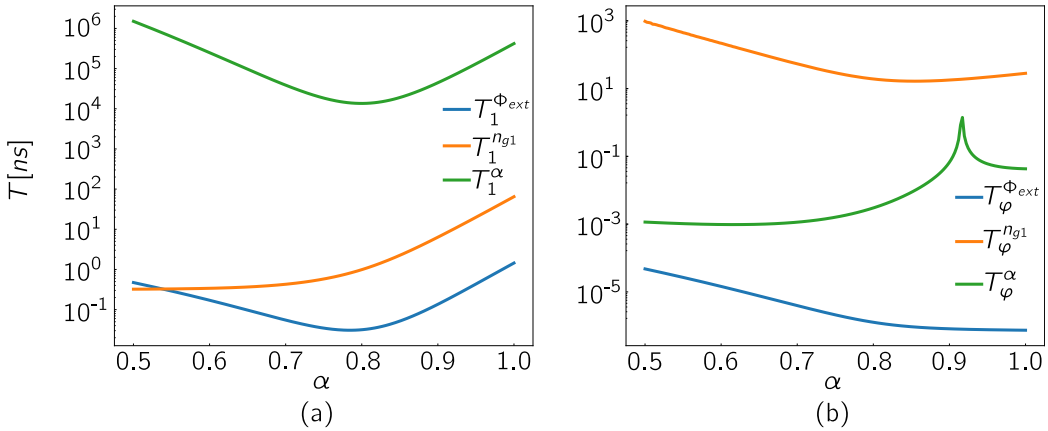

Figure 4.5: Coherence times for the Flensmon, with $E_J/E_C = 100$, $\phi_{ext} = 0.997\pi$. The dephasing due to flux noise is the limiting factor of the total decoherence time.

Chapter 5

Gradiometric Flensmon

The limiting factor of the Flensmon is the dephasing time due to fluctuations in external flux. To resolve this issue, a gradiometric design of the Flensmon is shown in this chapter. The idea is that the eigenstates still correspond to the current direction in a circuit, but now there are two loops. This way the global flux fluctuations should be evened out between the two loops. The currents will run opposite of each other in the two loops.

This design is showed in figure Figure 5.1. It should be noticed that there are once again three islands in this setup, resulting in two degrees of freedom. We call this setup the double loop Flensmon or gradiometric Flensmon.

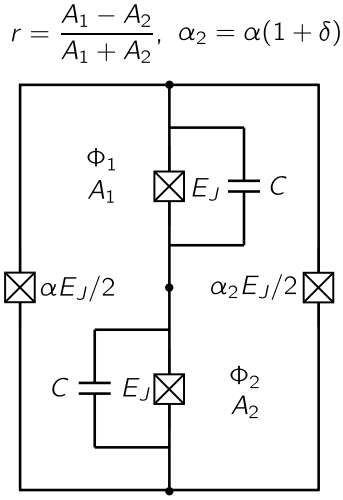

Figure 5.1: Circuit of gradiometric Flensmon. Φ_1 and Φ_2 denotes the flux through the left and right loop, while A_1 and A_2 are the areas. r is the ratio of the loop size in the circuit. α and δ is used to tune the outer Josphson junctions.

We have shunted the two middle islands to make both modes heavy. We omit the

Josephson capacitance of the other junctions as this capacitance is small compared to the capacitance of the shunt capacitors.

We write up the Lagrangian for the circuit in Figure 5.1,

$$\begin{aligned}\mathcal{L} = &\left(\frac{\Phi_0}{2\pi}\right)^2\left(\frac{C_{01}}{2}\dot{\phi_1}^2 + \frac{C_{02}}{2}\dot{\phi_2}\right) + E_J\cos(\phi_1) + E_J\cos(\phi_2)\\ &+\frac{1}{2}E_J\alpha\cos(-\phi_1+\phi_2+\Phi_1) + \frac{1}{2}E_J(1+\delta)\alpha\cos(\phi_1-\phi_2+\Phi_2),\end{aligned} \tag{5.1}$$

where we have used $\alpha_2 = \alpha(1+\delta)$. The usual Legendre transformation is made, we use that all capacitors are of equal size $C_{01} = C_{02} = C_s$. A charge offset is added on all islands $n_i \to (n_i - n_{gi})$,

$$\begin{aligned}\mathcal{H} = &4E_{Cs}\left((n_1-n_{g1})^2 + (n_2-n_{g2})^2\right) - E_J\cos(\phi_1) - E_J\cos(\phi_2)\\ &-\frac{1}{2}E_J\alpha\cos(-\phi_1+\phi_2+\Phi_1) - \frac{1}{2}E_J(1+\delta)\alpha\cos(\phi_1-\phi_2+\Phi_2).\end{aligned} \tag{5.2}$$

First, we assume that the same magnetic field is through the two loops, but the area of the loops may not be equal. We write the fluxes in terms of the global flux, Φ_G, and the difference in flux, Φ_D, due to different areas of the loops,

$$\begin{aligned}&\Phi_1 = A_1B = \Phi_G + \Phi_D, \quad \Phi_2 = A_2B = \Phi_G - \Phi_D,\\ &\frac{\Phi_D}{\Phi_G} = \frac{A_1 - A_2}{A_1 + A_2} \equiv r \Leftrightarrow \Phi_D = r\Phi_G\\ &\Phi_1 = (1+r)\Phi_G, \quad \Phi_2 = (1-r)\Phi_G.\end{aligned} \tag{5.3}$$

Furthermore, there can be a local flux through one of the loops due to either fluctuating spins in the circuit, or the magnetic field we apply is not uniform over the whole circuit. We write this as $\Phi_{1/2} = (1 \pm r)(\Phi_G \pm \Phi_L)$. The potential of the Hamiltonian can then be written,

$$\begin{aligned}V/E_J = &-\cos(\phi_1) - \cos(\phi_2) - \frac{1}{2}\alpha\cos(-\phi_1+\phi_2+(1+r)(\Phi_G+\Phi_L))\\ &-\frac{1}{2}(1+\delta)\alpha\cos(\phi_1-\phi_2+(1-r)(\Phi_G-\Phi_L)).\end{aligned} \tag{5.4}$$

We show the potential landscape and wave functions in Figure 5.2 with the parameters $E_J/E_C = 100, r = 0.005$ and $\Phi_G = 0.997\pi$. In this chapter Φ_G and Φ_L are the reduced fluxes and act as phases. Through this chapter the local flux Φ_L will be zero, we will only use it when calculating the spectrum due to the

local flux, and when finding coherence times with noise in the local flux. The one dimensional cut in Figure 5.2 shows that like the single loop Flensmon, the wave functions are delocalized in separate wells. The potential and wave functions are as we expect equal to that of the single loop Flensmon. The two states are still delocalized in separate wells.

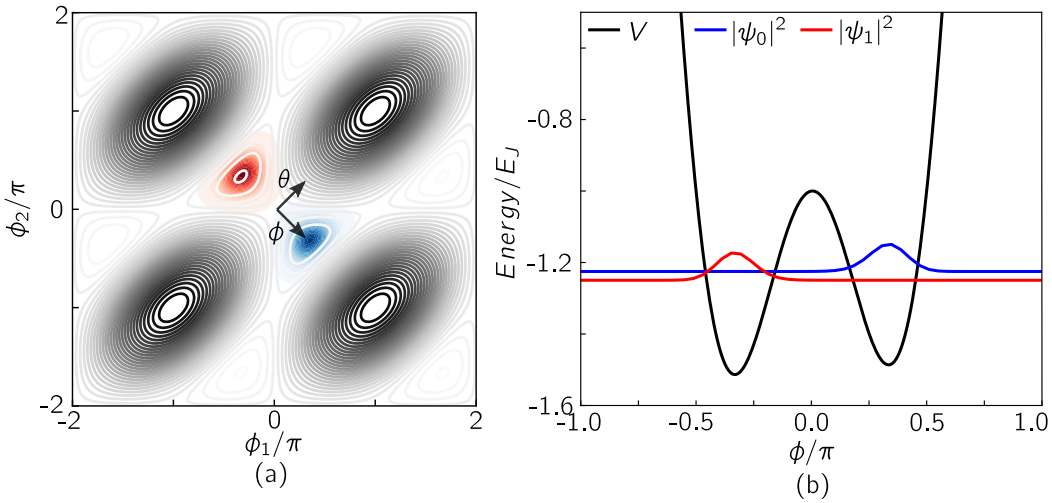

Figure 5.2: (a) Potential landscape of the Flensmon with $E_J/E_C = 100$ and $\alpha = 1$. The the basis with $2\phi = \phi_1 - \phi_2$ and $2\theta = \phi_1 + \phi_2$ is indicated. (b) One-dimensional cut of the ϕ mode, with the two qubit states shown. In both figures the external magnetic field is $\Phi_{ext} = 0.997\pi$ and $r = 0.005$, in order not to be in an artificial sweetspot. The energy splitting is due to area difference in the two loops.

We can find the spectrum with respect to charge fluctuations and the energy of the tunable junctions. The simulations are shown in Figure 5.3 where it is assumed that we can tune the two junctions in the same way simultaneously. The spectrums are comparable to the ones from Chapter 4, as expected. When only tuning one of the junctions the spectrum is flat, even when we go to quite different energies in the junctions. This is not true if we go further away from half flux quantum. In these simulations, we have $\Phi_G = 0.997\pi$, but further away it becomes more important that the junction energies are tuned precisely.
We wish to find a saddle point of the qubit frequency due to δ and Φ_G such that we can predict what δ should be if the two areas are of different sizes. We assume that each well can be approximated with two harmonic oscillators. The potential is rewritten in the ϕ and θ basis,

$$2\phi = \phi_1 - \phi_2, \quad 2\theta = \phi_1 + \phi_2, \tag{5.5}$$

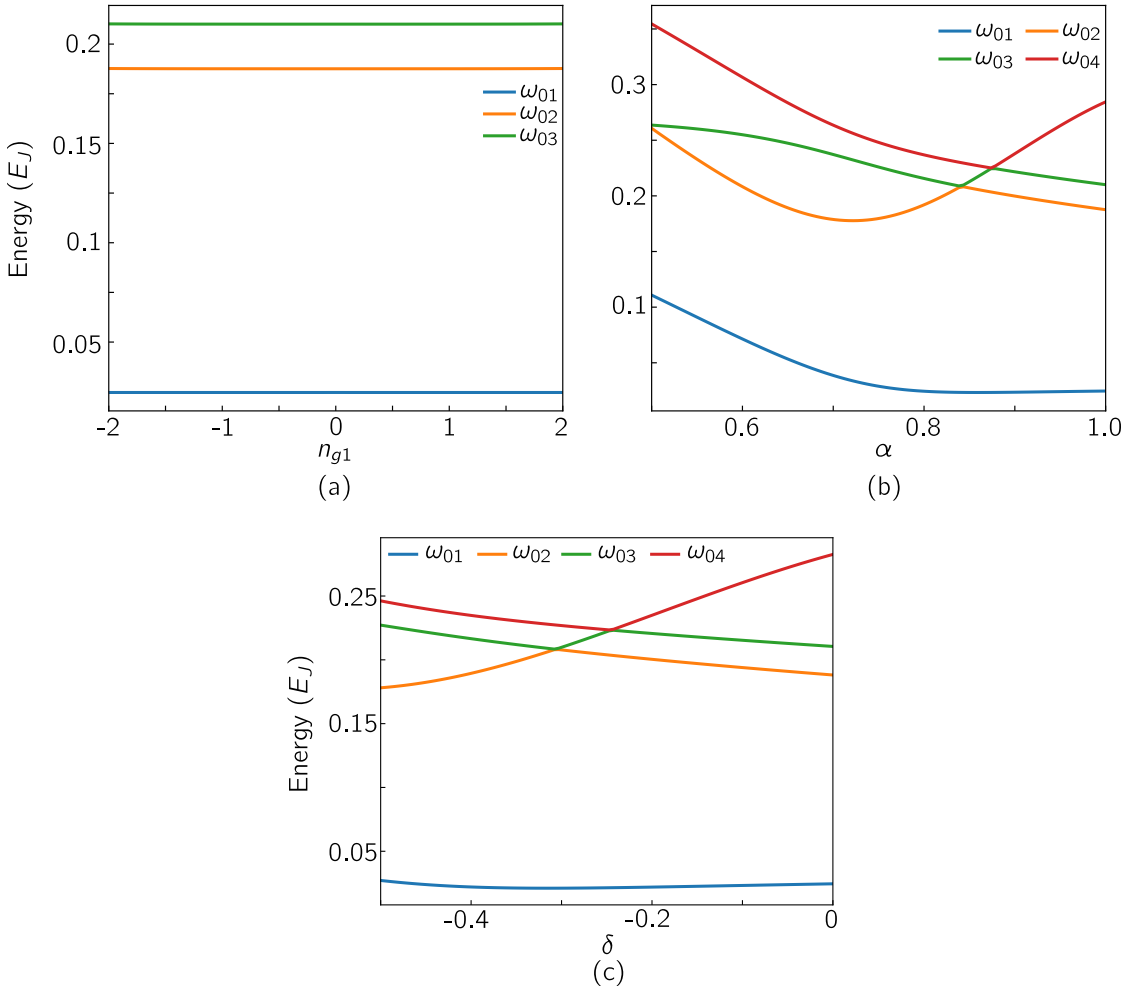

Figure 5.3: Spectrum of different external parameters. We have used $E_J/E_C = 100, r = 0.005, n_{g1} = 0, \alpha = 1$ and $\delta = 0$ in all simulations and then we vary one of them. (a) Varying the charge offset over junction 1, n_{g1}. (b) Varying the tunable junctions, α. (c) Varying only one of the tunable junctions, δ.

where the ϕ direction is where the double well is located. In this analysis $\Phi_L = 0$.

$$
\begin{aligned}
V/E_J &= -2\cos(\phi)\cos(\theta) - \frac{1}{2}\alpha(\mu - 2)\cos(2\phi) - \frac{1}{2}\eta\sin(2\phi), \\
\text{with } \mu &= \cos((1+r)\Phi_G) + (1+\delta)\cos((1-r)\Phi_G) + 2, \\
\eta &= \sin((1+r)\Phi_G) - (1+\delta)\sin((1-r)\Phi_G).
\end{aligned} \tag{5.6}
$$

V/E_J has minima in $\phi_0 = \pm\frac{\pi}{3}$ and $\theta_0 = 0$ when $r = \delta = 0$ and $\Phi_G = \pi$ ($\mu = 0$ and $\eta = 0$), and has the value $V/E_J = -\frac{3}{2}$. Now we are slightly away from perfect sized loops meaning $0 \neq r \ll 1$, the parameters we can vary are a tunable junction δ and the magnetic field Φ_G. This means $\mu \ll 1$ and $\eta \ll 1$. We wish to find the new minima by solving,

$$0 = \left.\frac{\partial V/E_J}{\partial \phi}\right|_{\theta=0,\phi=\pm\frac{\pi}{3}+\delta\phi},$$
$$\Leftrightarrow \delta\phi = \mp\frac{\sqrt{3}}{6}\mu - \frac{\eta}{6}, \tag{5.7}$$

Putting this into the potential we arrive at,

$$V_\pm/E_J = -\frac{3}{2} - \frac{3}{5}\mu \mp \frac{7\sqrt{3}}{12}\eta, \tag{5.8}$$

for $\mu, \eta \to 0$ we arrive at $V_\pm/E_J = -\frac{3}{2}$ as one would expect. We now find the curvature in the minima,

$$\left.\frac{\partial^2 V/E_J}{\partial \phi^2}\right|_{\theta=0,\phi=\pm\frac{\pi}{3}+\delta\phi} = 3 - \frac{5}{2}\mu \pm \frac{\sqrt{3}}{2}\eta,$$
$$\left.\frac{\partial^2 V/E_J}{\partial \theta^2}\right|_{\theta=0,\phi=\pm\frac{\pi}{3}+\delta\phi} = 1 + \frac{\mu}{2} \pm \frac{\eta}{2\sqrt{3}}. \tag{5.9}$$

To transform the number operator into this basis we use,

$$n_1 = \frac{1}{2}, \quad n_2 = \frac{1}{2}(n_\phi + n_\theta). \tag{5.10}$$

The kinetic term of the Hamiltonian in these coordinates are,

$$\mathcal{T} = E_{Cs}\left(2n_\phi^2 + 2n_\theta^2\right). \tag{5.11}$$

The approximate Hamiltonian becomes,

$$\mathcal{H} \approx 2E_{Cs}n_\phi^2 + \frac{E_J}{2}\left(3 - \frac{5}{2}\mu \pm \frac{\sqrt{3}}{2}\eta\right)\phi^2 + 2E_{Cs}n_\theta^2 + \frac{E_J}{2}\left(1 + \frac{\mu}{2} \mp \frac{\eta}{2\sqrt{3}}\right)\theta^2, \tag{5.12}$$

the energy eigenvalues of the approximate Hamiltonian are to first order,

$$\omega_{nm} = 2\sqrt{E_J E_{Cs}}\left(\sqrt{3}\left(1 - \frac{5}{12}\mu \pm \frac{\eta}{4\sqrt{3}}\right)(n + \frac{1}{2}) + \left(1 + \frac{\mu}{4} \mp \frac{\eta}{4\sqrt{3}}\right)(m + \frac{1}{2})\right), \tag{5.13}$$

where n and m denotes the excitations of ϕ and θ. The ground state has energy ω_{00-} while the first excited state has ω_{00+}. The qubit energy is then,

$$\omega_q = \left(\frac{\sqrt{3}-1}{2\sqrt{3}} \right) |\eta| \sqrt{E_J E_{Cs}}. \tag{5.14}$$

To find the saddle point we solve,

$$\begin{aligned} &\frac{\partial \omega_q}{\partial \delta} = 0, \quad \frac{\partial \omega_q}{\partial \Phi_G} = 0, \\ &1 + \delta = \frac{1+r}{1-r} \cos\left(\frac{r\pi}{1-r} \right) \approx 1 + 2r, \end{aligned} \tag{5.15}$$

we see that to flatten the band, and make it easier to tune to a sweet spot due to different areas of the two loops, we can tune the tunable junctions such that $\delta = 2r$.

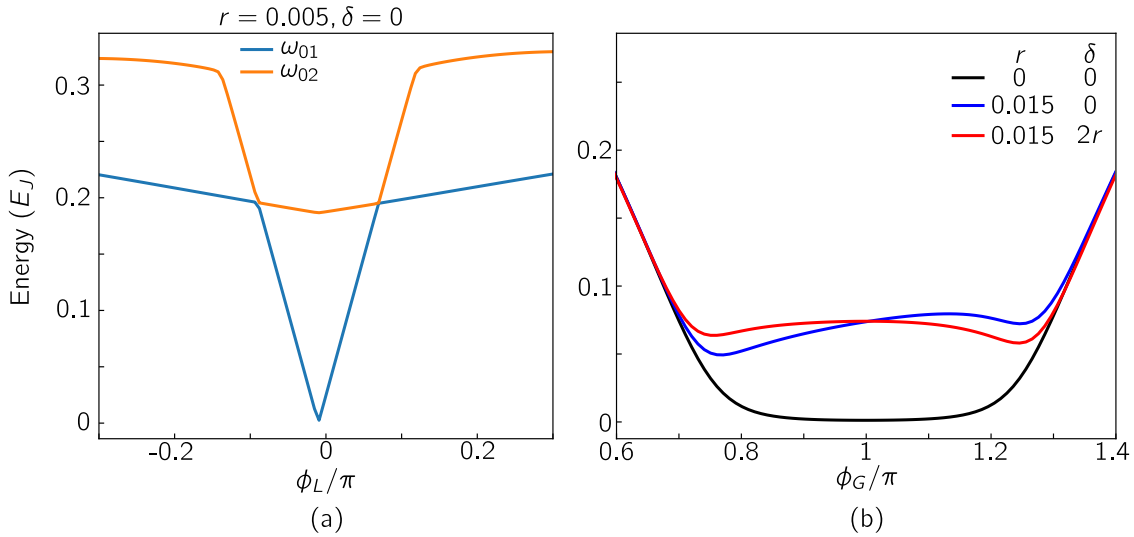

Figure 5.4: Spectrum as a function of flux variables in gradiometric Flensmon. (a) Varying local flux, the global flux is set to $\Phi_G = 0.997\pi$. The spectrum is linear. (b) Varying global flux. The black curve shows that the spectrum is exponentially flat if we have the perfect setup equal sized loops. Blue curve shows how diffrent loops areas results in splitting of energy and a more linear dispersion. Red curve shows a flat spectrum near half flux quantum if the right offset between the tunable junctions are made.

In Figure 5.4 the spectrum is simulated both as a function of local flux and global flux. We see in Figure 5.4(a) that the dispersion is linear due to the local flux. This is not odd as the geometry of the circuit does not protect against local

flux fluctuations. On the other hand, if we look at Figure 5.4(b) the black curve becomes exponentially flat around half flux quantum, $\Phi_G = \pi$. This curve is for the ideal setup where the two loops are of equal size, which is not realistic, but Kou et al. [30] succeeded in making a gradiometric setup for another qubit, here they could make the areas the same size up to half a percent. Future simulations with the gradiometric setup will have $r = 0.005$. The blue curve in Figure 5.4b is a setup where the loop size differ with 1.5%. We chose for this simulation a larger loop area difference as it becomes clearer what happens to the spectrum. Here we see that the qubit state energies split slightly and a linear slope appears. Last we try and correct for the loops not being the same size, by tuning the other tunable junction with $\delta = 2r$ as suggested from our analysis earlier. The slope flattens around half flux quantum, which should result in a better dephasing time.

Coherence times

For the gradiometric Flensmon we look at the same external noise parameters as in Chapter 4, with the addition of the local flux noise. The coherence times are calculated in a similar way as in the previous chapter. The pure dephasing times are comparable to Equations (4.25), (4.29) and (4.33) for global flux noise, charge noise and noise from the tunable junctions. The dephasing due to local flux noise is found similarly and looks close to Equation (4.25), just where the derivatives are with respect to local flux, Φ_L. For the depolarization times, we need to take the derivatives of the Hamiltonian. We will not show all calculations, but just list the transition rates used to find T_1^λ, where λ is the external noise parameter.

$$\Gamma_1^{\Phi_G} = \Bigg| \langle 1| \left(\frac{1}{2}\alpha(1+r)E_J \sin\left(-\phi_1+\phi_2+(1+r)(\Phi_G+\Phi_L)\right) \right.$$
$$\left. + \frac{1}{2}(1+\delta)\alpha(1-r)E_J \sin\left(\phi_1-\phi_2+(1-r)(\Phi_G-\Phi_L)\right) \right) |0\rangle \Bigg|^2 (2\pi)^3 \frac{A_\Phi^2}{\Phi_0^2|\omega_q|}, \tag{5.16}$$

$$\Gamma_1^{n_{g1}} = |\langle 1| (n_1 - n_{g1}) |0\rangle|^2 (8E_C)^2 \frac{2\pi\left(\frac{A_{n_g}}{2e}\right)^2}{|\omega_q|}, \tag{5.17}$$

$$\Gamma_1^{\alpha} = \Bigg| \langle 1| \left(\frac{1}{2}\cos\left(-\phi_1+\phi_2+(1+r)(\Phi_G+\Phi_L)\right) \right.$$
$$\left. + \frac{1}{2}(1+\delta)\cos\left(\phi_1-\phi_2+(1-r)(\Phi_G-\Phi_L)\right) \right) |0\rangle \Bigg|^2 \left(\frac{\Phi_0}{2\pi}\right)^2 \frac{2\pi A_{I_{C3}}^2}{|\omega_q|}, \tag{5.18}$$

$$\Gamma_1^{\Phi_L} = \Bigg| \langle 1| \left(\frac{1}{2}\alpha(1+r)E_J \sin\left(-\phi_1+\phi_2+(1+r)(\Phi_G+\Phi_L)\right) \right.$$
$$\left. - \frac{1}{2}(1+\delta)\alpha(1-r)E_J \sin\left(\phi_1-\phi_2+(1-r)(\Phi_G-\Phi_L)\right) \right) |0\rangle \Bigg|^2 (2\pi)^3 \frac{A_\Phi^2}{\Phi_0^2|\omega_q|}. \tag{5.19}$$

The same noise amplitudes as in the previous chapter are used $A_\Phi = 10^{-6}\Phi_0$, $A_{n_g} = 10^{-4}e$ and $A_{I_{C3}} = 10^{-7}\frac{2\pi\alpha E_J}{\Phi_0}$.

All coherence times simulated for the gradiometric Flensmon are shown in Figure 5.5. We have used the usual parameters with $E_J/E_C = 100, \Phi_G = 0.997\pi$, $\Phi_L = 0$ and $r = 0.005$. As the limiting coherence time is no longer the global flux of the system, the gradiometric design is indeed protected against fluctuations in global flux. However, local flux deviations can still be a problem as this is the limiting coherence time. If we take the gradiometric Flensmon to the limit of the CSFQ regime, the limiting depolarization time is due to charge noise and not flux noise anymore. In Figure 5.5c we compare the single loop and gradiometric designs. Note how the dephasing time in the single loop Flensmon is slightly worse than in the gradiometric setup, even though it is in the same parameter choice.

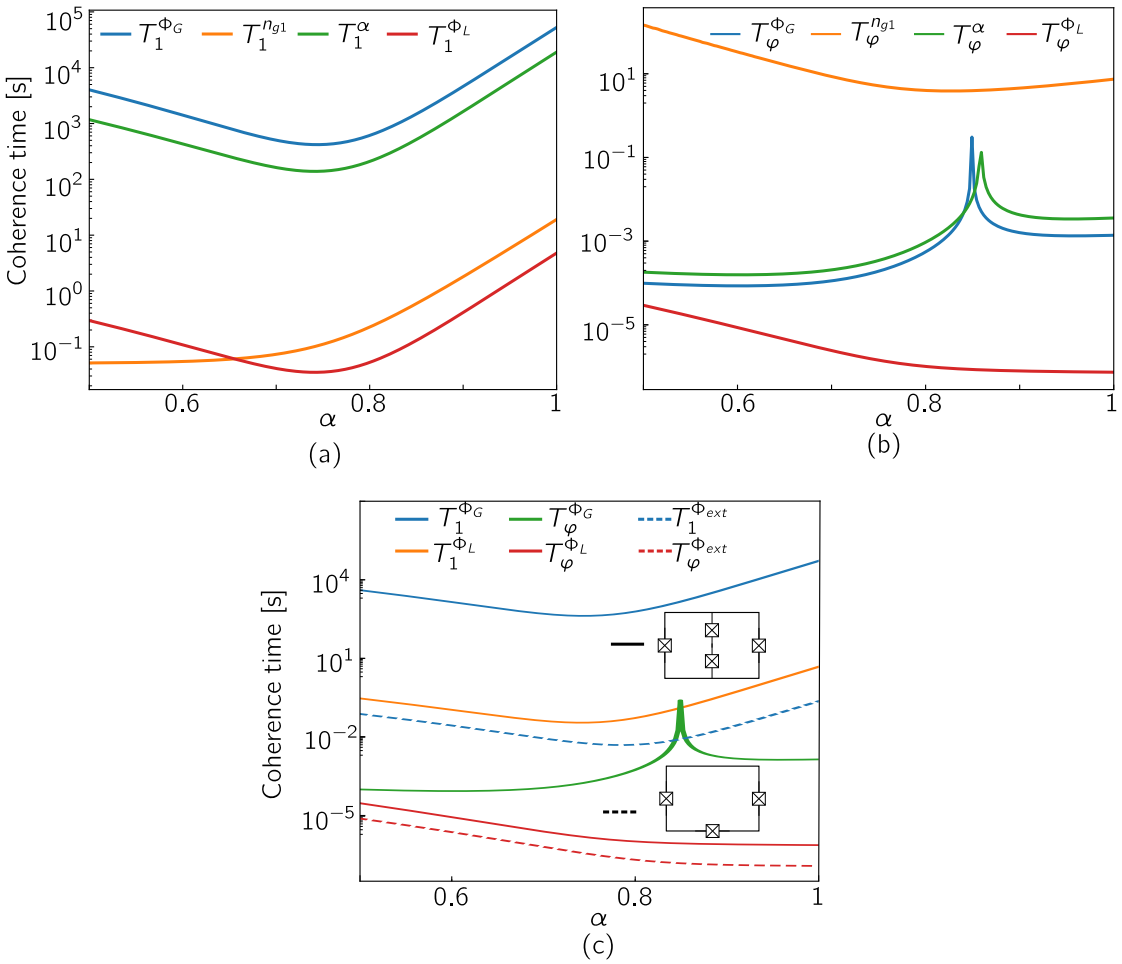

Figure 5.5: Coherence times of the gradiometric Flensmon, with $E_J/E_C = 100, \Phi_G = 0.997\pi, \Phi_L = 0$ and $r = 0.005$, as a function of α. (a) Depolarization times, T_1. The limiting depolarization time is due to local flux noise for $\alpha > 0.65$. (b) Pure dephasing times, T_φ. The limiting dephasing time is due to local flux noice. We see that the global flux noise has a good dephasing time. (c) Comparison of coherence times due to flux noise, between the single loop Flensmon and gradiometric Flensmon. Dashed curves are single loops, full curves are gradiometric.

Chapter 6

Qubit gates

The Bloch sphere is often used to represent a qubit state. This has already been used earlier in this thesis. In this representation $|0\rangle$ and $|1\rangle$ are on the South and North pole on the z-axis. Any superposition can be represented as a vector pointing to a point on the surface of the Bloch sphere.

To manipulate a qubit, rotations are made on the Bloch sphere and can be made around any axis. Figure 6.1 shows three arrows which represent a π rotation around the x-, y- and z-axes. To be able to get to any point on the Bloch sphere, only two of the rotations are needed. It is simple to show that by a combination of rotations about the x- and z-axis, one can generate rotations about the y-axis. Rotations on a single qubit are called single qubit gates, and to make all rotations on the Bloch sphere, at least two different single qubit gates are needed.

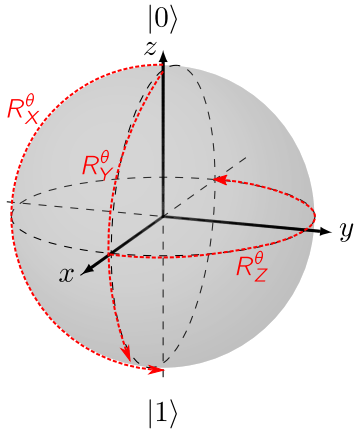

Figure 6.1: Rotations about the x-, y- and z-axis are shown in the Bloch sphere. All three arrows if followed from start to end represent a $\theta = \pi$ rotation about the axis indicated.

To make a quantum computer one also needs the qubits to be coupled in order to interact between qubits. In a system with two qubits that are coupled, two

qubit gates can be used to entangle the states. For the whole coupled system it is convenient if the coupling can be turned on and off. This will make it possible to operate single qubits without operating on the other qubits in the system. For a quantum computer to make all possible gate operations one needs two different single qubit gates and one two qubit gate. This makes a universal set of gates.

This chapter focuses on how simple quantum gates can be implemented on the Flensmon. This is not a thorough analysis of the fastest and most optimal gates, but rather simulations and arguments on how these gates are possible. We will show that it is possible to make the required two single qubit gates and one two qubit gate.

Single qubit gates

Most systems that are used for a qubit, have a lot of states outside the computational subspace. The same goes for the Transmon and the Flensmon. For simplicity, we will for now assume we have a system that can be modeled as a spin in order to introduce how one can make simple single qubit gates.

We start with a system which is modeled as a spin with Hamiltonian, H_0, for the qubit, and a driving term, H_d, which is coupled to the system,

$$H = -\frac{\omega_q}{2}\sigma_z + \Omega(t)\cos(\omega_d t + \phi)\sigma_x, \tag{6.1}$$

$$\tag{6.2}$$

where ω_q is the qubit frequency, $\Omega(t)$ is the drive amplitude, ω_d is the drive frequency and ϕ is the phase of the signal we drive the system with. The driving term is a time-dependent term in the Hamiltonian. We change to the interaction picture and find the interaction term of the Hamiltonian. The system is driven with the qubit frequency $\omega_d = \omega_q$,

$$H_{int} = \mathrm{e}^{iH_0 t} H_d \mathrm{e}^{-iH_0 t}, \tag{6.3}$$

$$= \Omega(t)\cos(\omega_q t + \phi)\begin{pmatrix} 0 & \mathrm{e}^{i\omega_q t} \\ \mathrm{e}^{-i\omega_q t} & 0 \end{pmatrix}, \tag{6.4}$$

$$= \frac{\Omega(t)}{2}\begin{pmatrix} 0 & \mathrm{e}^{2i\omega_q t}\mathrm{e}^{i\phi} + \mathrm{e}^{-i\phi} \\ \mathrm{e}^{-2i\omega_q t}\mathrm{e}^{-i\phi} + \mathrm{e}^{i\phi} & 0 \end{pmatrix}. \tag{6.5}$$

The rotating wave approximation (RWA) is used where we discard all exponentials with $2i\omega_q$, together with $\mathrm{e}^{i\theta\sigma_i} = \cos\theta + i\sin\theta\sigma_i$,

$$H_{int} = \frac{\Omega(t)}{2}\left[\begin{pmatrix} 0 & \cos\phi \\ \cos\phi & 0 \end{pmatrix} + \begin{pmatrix} 0 & -i\sin\phi \\ i\sin\phi & 0 \end{pmatrix}\right] \tag{6.6}$$

$$= \frac{\Omega(t)}{2}[\cos\phi\sigma_x + \sin\phi\sigma_y]. \tag{6.7}$$

With the Hamiltonian derived in the interaction picture, we can construct the time evolution operator in the interaction picture,

$$U_I(T) = 1 - \int_0^T \mathrm{d}t\ H_{int}U_I(t) \tag{6.8}$$

we approximate the Dyson series to first order,

$$U_I(T) \approx \mathrm{e}^{-i\int_0^T \mathrm{d}t\ H_{int}} = \mathrm{e}^{-i\int_0^T \mathrm{d}t\frac{\Omega(t)}{2}[\cos\phi\sigma_x+\sin\phi\sigma_y]} = \mathrm{e}^{-i\int_0^T \mathrm{d}t\frac{\Omega(t)}{2}[I\sigma_x+Q\sigma_y]}, \tag{6.9}$$

this is called IQ-mixing where $I = \cos\phi$ and $Q = \sin\phi$. By choosing ϕ we can contruct the desired combination of rotations. In order to make a bit flip from $|0\rangle$ to $|1\rangle$, we could make $\phi = 0$; then the time evolution operator would be,

$$U_I(T) = \mathrm{e}^{-\frac{i}{2}\int_0^T \mathrm{d}t\ \Omega(t)\sigma_x}, \tag{6.10}$$

and driving the system for a time T such that $\int_0^T \mathrm{d}t\ \Omega(t) = \pi$, means we are going to apply a π-pulse,

$$U_I(T) = \mathrm{e}^{-i\frac{\pi}{2}\sigma_x} = -i\sigma_x, \tag{6.11}$$

applying this to the ground state $|0\rangle$ flips the bit to $-i\,|1\rangle$. The $-i$ is just a global phase and can be ignored in this single qubit example. We can define the angle which is rotated, to be $\theta \equiv \int_0^T \mathrm{d}t\ \Omega(t)$. In this example, it is analog to the angle rotated around the x-axis. This is an example of how to apply a Pauli-X gate, also known as a NOT gate, the phase of the drive signal could be tuned such that $\phi = \frac{\pi}{2}$, which will result in a Pauli-Y gate. These gates can together operate as Pauli-Z gates. If the qubit has good enough anharmonicity the Hamiltonian of the qubit can be truncated to the form of Equation (6.1).

The Flensmon has degenerate eigenstates when $\alpha = 1$. Because we have a tunable junction in the Flensmon, we can change the potential of the eigenstates of the system. We want to adiabatically change α to lower the barrier between the

two wells. This way we open an overlap and split the energies of the qubit states. The anharmonicity is reasonable in the Flensmon therefore we are now able to model the system as a two level system where a drive is coupled. The drive can be coupled to the system capacitively. There are of course better and faster ways of making a gate for a Flensmon. One way is to make use of the higher levels to go over the barrier [31], but we will only focus on the fact that it is possible to make at least two single qubit gates, even though is not the fastest way of doing it.

Two qubit gates

To make two qubit gates, we need to couple two qubits. To couple the modes of the qubits, one can think of a capacitive coupling or an inductively coupling. We will propose to use capacitors as the coupling is much stronger than the inductive coupling. The schematic of the circuit can be seen in Figure 6.2. Similar physics applies to the gradiometric Flensmon, but we have focused on the single loop Flensmon.

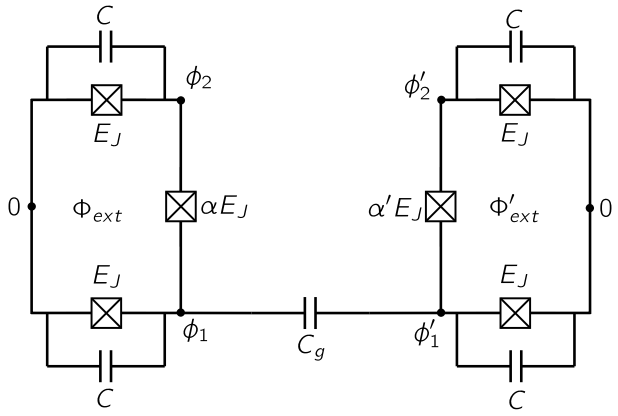

Figure 6.2: Schematic of two coupled Flensmon qubits. α and α' denotes that the junctions are tunable.

The Lagrangian for the total circuit can be written as usual,

$$\begin{aligned}\mathcal{L} = &\frac{C}{2}\dot{\phi}_1^2 + \frac{C}{2}\dot{\phi}_2^2 + \frac{C}{2}\dot{\phi}_1'^2 + \frac{C}{2}\dot{\phi}_2^2 + \frac{C_g}{2}\left(\dot{\phi}_1 - \dot{\phi}_1'\right)^2 \\ &+ E_J\cos\phi_1 + E_J\cos\phi_2 + \alpha E_J\cos\left(\phi_1 - \phi_2 + \phi_{ext}\right) \\ &+ E_J\cos\phi_1' + E_J\cos\phi_2' + \alpha' E_J\cos\left(\phi_1' - \phi_2' + \phi_{ext}'\right),\end{aligned} \tag{6.12}$$

doing the Legendre transformation we arrive at the Hamiltonian, where we have used $C = \frac{e^2}{2E_C}, C_g = \frac{e^2}{2E_{Cg}}$ and $q_i = 2en_i$,

$$
\begin{aligned}
\mathcal{H} = \frac{4E_C}{\left(\frac{2}{E_{Cg}}+\frac{1}{E_C}\right)}\Bigg[&\left(\frac{1}{E_C}+\frac{1}{E_{Cg}}\right)n_1^2+\left(\frac{1}{E_C}+\frac{2}{E_{Cg}}\right)n_2^2 \\
&+\left(\frac{1}{E_C}+\frac{1}{E_{Cg}}\right)n_1'^2+\left(\frac{1}{E_C}+\frac{2}{E_{Cg}}\right)n_2'^2 \\
&+\frac{2}{E_{Cg}}n_1n_1'\Bigg] \\
&-E_J\cos\phi_1-E_J\cos\phi_2-\alpha E_J\cos\left(\phi_1-\phi_2+\phi_{ext}\right) \\
&-E_J\cos\phi_1'-E_J\cos\phi_2'-\alpha' E_J\cos\left(\phi_1'-\phi_2'+\phi_{ext}'\right). \qquad (6.13)
\end{aligned}
$$

The Hamiltonian is a sum of the two qubits individual Hamiltonians, where the kinetic energies of the system have been renormalized due to the extra capacitor between them, but where an extra term is proportional to n_1n_1' arises due to the coupling between the two circuits. This coupling can entangle the two qubit states if the two systems' wave functions overlap. The total system of the circuit in Figure 6.2 is truncated into the lowest four energy eigenstates. They are called $|00\rangle, |10\rangle, |01\rangle$ and $|11\rangle$ where $|ij\rangle = |i\rangle \otimes |j\rangle$. Imagine an experiment where the two qubits on either side of the coupling capacitor are identical, and we can tune α and α' precisely the same way, then if the qubits are not interacting the states $|10\rangle$ and $|01\rangle$ would be degenerate for all $\alpha = \alpha'$. The interaction caused by the n_1n_1' term will, if an overlap is created between the wave functions $|10\rangle$ and $|01\rangle$, cause an energy splitting between these states. The Hamiltonian is solved numerically and the eigenstates and energies of the system are found. The energy eigenvalues are shown in Figure 6.3 with two different coupling capacitors. In Figure 6.3(a) a smaller capacitance is used with charging energy $E_{Cg}/E_J = 0.1$, and in Figure 6.3(b) a larger capacitance with charging energy $E_{Cg}/E_J = 0.01$. For $\alpha = 1$ the two qubits are degenerate and are presumably not interacting. When α and α' in both qubits are simultaneously lowered, an energy splitting occurs.
From Figure 6.3 it is hard to conclude more than that the energy splitting between the states $|10\rangle$ and $|01\rangle$ split in energy, and that the splitting and energies depend on the coupling capacitor. In Figure 6.4 the splitting at $\alpha = \alpha' = 0.6$ is showed where the charging energy of the coupling capacitor is varied. It is easy to see here that the splitting indeed gets larger when the capacitance is increased.

The previous discussion concludes that an energy splitting occurs between the degenerate states $|10\rangle$ and $|01\rangle$. We model two identical qubits as two non-interacting systems, by splitting the Hamiltonian in Equation (6.13) into $\mathcal{H} = H_A + H_B + H_{int}$, where A and B denotes the left and right qubit, while H_{int} is the coupling in Figure 6.2,

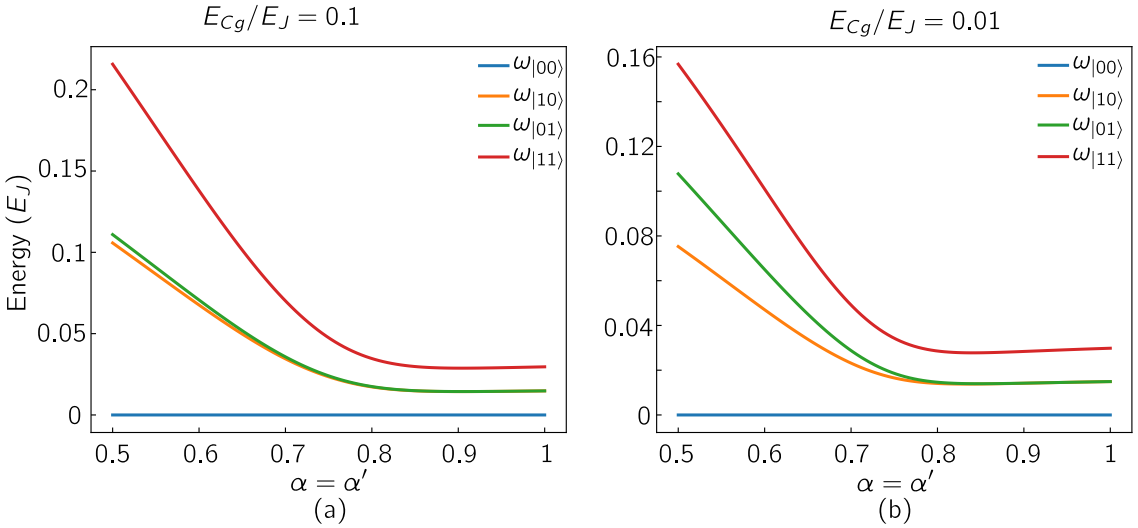

Figure 6.3: The lowest four energies of two identical coupled Flensmon with (a) $E_{Cg}/E_J = 0.1$ (b) $E_{Cg}/E_J = 0.01$. The energy of the ground state has been fixed to 0. In both cases an energy splitting between $|10\rangle$ and $|01\rangle$ occurs. The coupling capacitor between the plates sets the energies and how much they split. The system with the large capacitor (b) has a larger energy splitting.

$$H_{int} = \frac{8E_C}{E_{Cg}\left(\frac{2}{E_{Cg}} + \frac{1}{E_C}\right)} n_1 n_1'. \tag{6.14}$$

In Figure 6.5 the system is solved for each qubit by itself and then the eigenstates of the full system is made with tensor products of the uncoupled system, $|ij\rangle = |i\rangle \otimes |j\rangle$. This system is solved using a large capacitance between the qubits, $E_{Cg}/E_J = 0.01$, which as we saw leads to a larger energy splitting in Figure 6.4. The six overlaps simulated in Figure 6.5 are the six different transitions that can occur within the computational subspace of the two coupled qubits. The overlaps tell us which transitions are allowed. The allowed transitions are only between $|00\rangle \leftrightarrow |11\rangle$ and $|10\rangle \leftrightarrow |01\rangle$. The simulations are done with both Figure 6.5(a) tunable junctions are lowered at the same time, and Figure 6.5(b) that only one of the tunable junctions is varied. It is clear that in order to make an overlap between different states, both of the junctions needs to be tuned to a value between $\alpha = \alpha' = 0.5$ and $\alpha = \alpha' = 0.7$. This feature allows one to only couple the qubits when the tunable junctions are tuned simultaneously, and by only tuning one of them, single qubit gates can be done without interfering with the other qubit.

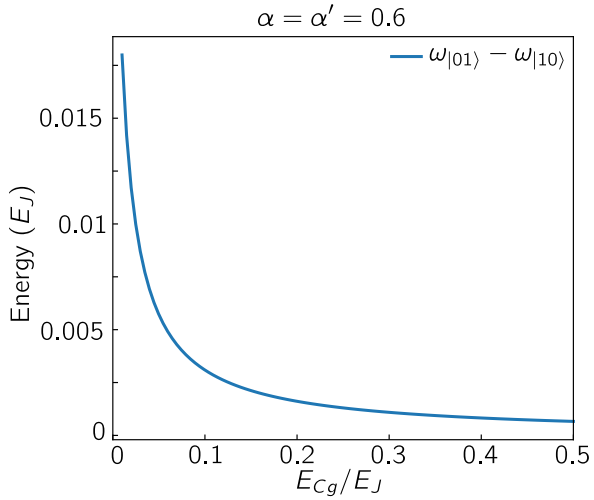

Figure 6.4: The energy splitting between $|10\rangle$ and $|01\rangle$ in a system of two identical coupled Flensmons with $\alpha = \alpha' = 0.6$. The coupling capacitor between the two qubits is varied, and a larger coupling capacitor between the qubits gives a larger energy splitting.

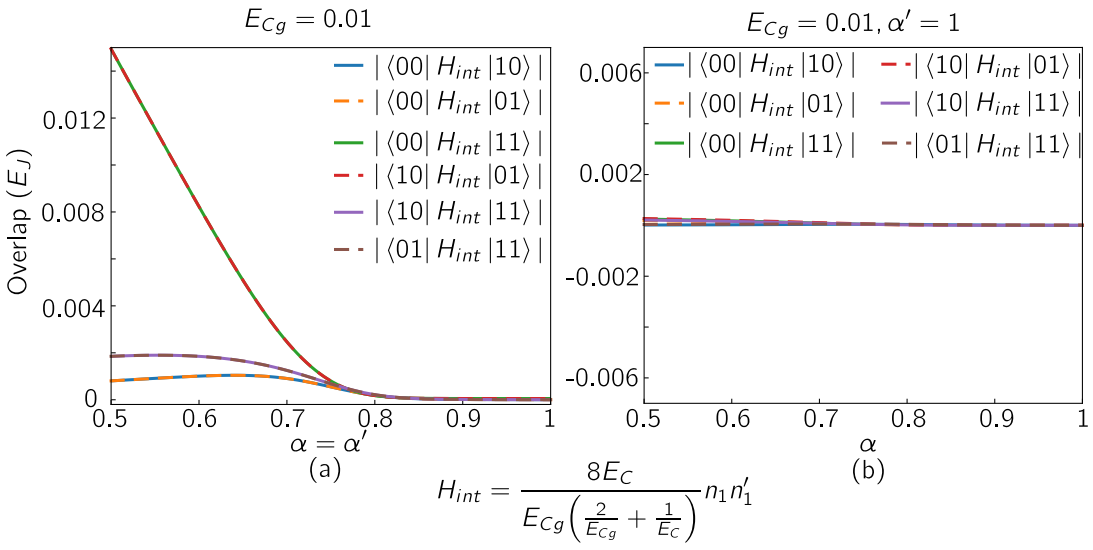

Figure 6.5: Overlap between different qubit states. (a) Barrier lowered in both qubits at the same time. The overlap opens for transitions between $|00\rangle \leftrightarrow |11\rangle$ and $|10\rangle \leftrightarrow |01\rangle$. (b) Only one barrier is lowered, the overlap does not open and allows for single qubit operations without interfering with the other qubit.

Chapter 7

Qubit readout

To use qubits for quantum computation, one needs to measure the state of each qubit. This chapter will be a brief overview of how to readout and measure the state of a qubit with good anharmonicity and non-degenerate energies of the qubit subspace. One of the most used readout techniques is dispersive readout, this is one option for the readout of the Flensmon qubit. Here linear resonators are used to measure the qubit.

Dispersive readout

To measure a qubit using dispersive readout, the qubit has to be coupled to a linear resonator, in our case it is an LC-oscillator. A schematic is shown in Figure 7.1.

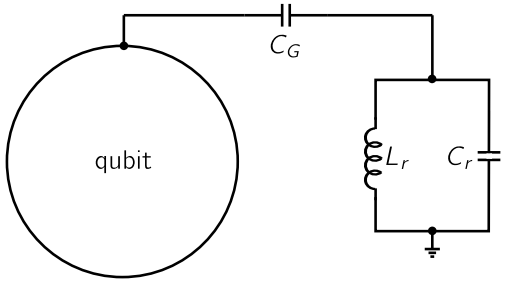

Figure 7.1: The circuit used for a dispersive readout. Any qubit coupled capacitively to an LC-oscillator also called linear resonator. The qubit is a superconducting qubit truncated into a two level system with qubit frequency ω_q. The resonator has frequency $\omega_r = \sqrt{\frac{E_{Cr}}{L_r}}$, where the charging energy depends on the capacitor in the resonator, $E_{Cr} = \frac{e^2}{2C_r}$, and L_r is the inductance of the resonator.

Here the qubit shown could be any two level system with non-degenerate eigenenergies and with a good anharmonicity. The qubit is coupled to the oscil-

lator capacitively. The qubit has qubit frequency, ω_q, and anharmonicity a. The resonator has frequency $\omega_r = \sqrt{\frac{E_{Cr}}{L_r}}$, where the charging energy depends on the capacitor in the resonator, $E_{Cr} = \frac{e^2}{2C_r}$, and L_r is the inductance of the resonator.

The qubit in Figure 7.1 is assumed to be truncated into a two level system coupled to the linear resonator. In the RWA the Jaynes-Cummings Hamiltonian [15, 19, 32–34] can be written for the system,

$$H_{JC} = \frac{\omega_q}{2}\sigma_z + \omega_r b^\dagger b + g\big(\sigma_+ b + \sigma_- b^\dagger\big), \tag{7.1}$$

where $b^\dagger$ and b are creation and annihilation operators for the resonator, g is the coupling between the qubit and oscillator and $\sigma_\pm = \sigma_x \pm i\sigma_y$. The detuning between the qubit and resonator is defined to be $|\Delta| \equiv |\omega_q - \omega_r|$, and the dispersive shift is defined, $\chi = g^2/|\Delta|$, if the qubit is a pure two level system. When the resonator and qubit are detuned from each other and $g \ll |\Delta|$, the system is in the dispersive regime. The Jaynes-Cummings Hamiltonian (Equation (7.1)) can be approximated in the dispersive regime [15, 16, 19] to the dispersive Hamiltonian,

$$H_{disp} = (\omega_r + \chi\sigma_z)b^\dagger b + \frac{1}{2}\omega_q\sigma_z, \tag{7.2}$$

taking the second excited state into account the dispersive shift is [15, 19],

$$\chi = -\frac{g_{01}^2}{|\Delta|}\left(\frac{1}{1 + |\Delta|/a}\right), \tag{7.3}$$

where $a = \omega_{12} - \omega_q$ is the anharmonicity, with ω_{12} the energy difference between the first and second excited states, g_{01} is the coupling between the computational subspace and the resonator.

The dispersive Hamiltonian in Equation (7.2) can be interpreted in two ways, either as a shift of the qubit frequency induced by fluctuations in the photon number of the resonator or as a pull by the qubit on the resonator frequency, $\omega_r \to \omega_r \pm \chi$, where the pull is determined by which state the qubit is in. The latter interpretation is used when doing a dispersive readout. If the fluctuations of photons in the resonator are low, then a dispersive readout is possible by measuring the resonator frequency and seeing if the peak is shifted by $\pm\chi$.

This scheme can be used to readout the qubit state of the Flensmonif the qubit is in the regime where the energy eigenvalues are split. Depending on how large an energy splitting is needed for the readout, α is adiabatically tuned to a value between 0.5 and 0.7. The energy splitting depends on the coupling, between the qubit and resonator. After readout, α is changed adiabatically back to $\alpha = 1$.

Chapter 8

Conclusion and Outlook

This thesis has explored the Flensmon qubit. The qubit has been characterized by coherence times. The dephasing of the qubit is a problem in the single loop Flensmon due to flux noise through the loop. To engineer a solution to this problem, another loop is made and by having two loops, the dephasing time due to global flux noise has been increased. The dephasing due to local flux noise is still a problem and is hard to improve in this qubit. However, with improvements of the wires in the circuits, hopefully, the local flux noise from magnetic dipoles is less significant. The qubit is designed to have a long depolarization time, and it is indeed not the limiting factor. The anharmonicity of the Flensmon is also very good, even in the single well limit where $\alpha = 0.5$.

The Flensmon can be manipulated and measured. This thesis has shown that by tuning α in the Flensmon one can split the eigenenergies and make it possible to rotate the qubit in the Bloch sphere using a drive pulse coupled to the circuit. By using IQ-mixing the state can be rotated around two different axes, and by that make any single qubit gate. We have shown that by capacitively coupling two Flensmonqubits we can entangle them. This generates a charge-charge term between the qubits. Lowering α in both qubits simultaneously two wave functions overlap. Within the computational subspace of the two qubits, the overlap between $|10\rangle$ and $|01\rangle$ together with $|00\rangle$ and $|11\rangle$ becomes non-zero. The other transitions are prevented as the overlaps are suppressed. By adiabatically lowering α in both qubits a gate can be realized by driving the system. To manipulate only one qubit at a time, only the α associated with that qubit is lowered. Then one can do single qubit gates without affecting the other qubit. The readout of the qubit is done by again lowering α and splitting the eigenenergies of the qubit. This allows a dispersive readout by coupling the qubit to a linear resonator. The state of the qubit determines how the dispersive shift affects the resonator fre-

quency, and the state of the qubit can be measured. In the qubit gate and measurement chapters, it has only been argued that the different techniques are ways of doing gates and measurement, but the time of a gate or a measurement is not done in this thesis.

The work in progress is a full proposal for the Flensmon. Here the coherence times will be combined with simulations of single and two qubit gates. This analysis will include the leakage out of the computational subspace together with the time it takes to make the simple gates proposed in this thesis. We will furthermore simulate the dispersive readout to estimate the readout time of the Flensmon. A more thorough analysis of effecient gates will also be conducted. Here the thought is to use optimal control theory [31] whereby using the higher excited levels we can make faster gape operations. Hopefully, the Flensmon will be in the laboratory in the near future.

It would also be interesting to look into using the Flensmon as a tunable coupler between two other qubits. It has the right properties when two Flensmons are coupled together, and we might be able to use the same physics to construct a tunable coupler.

References

[1] John Preskill. Quantum computing 40 years later. *arXiv:2106.10522 [quant-ph]*, June 2021. arXiv: 2106.10522.

[2] Richard P Feynman. *Simulating physics with computers*. 1981.

[3] Peter W. Shor. Polynomial-Time Algorithms for Prime Factorization and Discrete Logarithms on a Quantum Computer. *SIAM Journal on Computing*, 26(5):1484–1509, October 1997. arXiv: quant-ph/9508027.

[4] Maximillian Zinner, Florian Dahlhausen, Philip Boehme, Jan Ehlers, Linn Bieske, and Leonard Fehring. Quantum computing's potential for drug discovery: Early stage industry dynamics. *Drug Discovery Today*, 26(7):1680–1688, July 2021.

[5] Colin D. Bruzewicz, John Chiaverini, Robert McConnell, and Jeremy M. Sage. Trapped-Ion Quantum Computing: Progress and Challenges. *Applied Physics Reviews*, 6(2):021314, June 2019. arXiv: 1904.04178.

[6] Yunfei Wang, Jianfeng Li, Shanchao Zhang, Keyu Su, Yiru Zhou, Kaiyu Liao, Shengwang Du, Hui Yan, and Shi-Liang Zhu. Efficient quantum memory for single-photon polarization qubits. *Nature Photonics*, 13(5):346–351, May 2019.

[7] David P. DiVincenzo and IBM. The Physical Implementation of Quantum Computation. *Fortschritte der Physik*, 48(9-11):771–783, September 2000. arXiv: quant-ph/0002077.

[8] András Gyenis, Agustin Di Paolo, Jens Koch, Alexandre Blais, Andrew A. Houck, and David I. Schuster. Moving beyond the Transmon: Noise-Protected Superconducting Quantum Circuits. *PRX Quantum*, 2(3):030101, September 2021.

[9] Frank Arute, Kunal Arya, Ryan Babbush, Dave Bacon, Joseph C. Bardin, Rami Barends, Rupak Biswas, Sergio Boixo, Fernando G. S. L. Brandao, David A. Buell, Brian Burkett, Yu Chen, Zijun Chen, Ben Chiaro, Roberto Collins, William Courtney, Andrew Dunsworth, Edward Farhi, Brooks Foxen, Austin Fowler, Craig Gidney, Marissa Giustina, Rob Graff, Keith Guerin, Steve Habegger, Matthew P. Harrigan, Michael J. Hartmann, Alan Ho, Markus Hoffmann, Trent Huang, Travis S. Humble, Sergei V. Isakov, Evan Jeffrey, Zhang Jiang, Dvir Kafri, Kostyantyn Kechedzhi, Julian Kelly, Paul V. Klimov, Sergey Knysh, Alexander Korotkov, Fedor Kostritsa, David Landhuis, Mike Lindmark, Erik Lucero, Dmitry Lyakh, Salvatore Mandrà, Jarrod R. McClean, Matthew McEwen, Anthony Megrant, Xiao Mi, Kristel Michielsen, Masoud Mohseni, Josh Mutus, Ofer Naaman, Matthew Neeley, Charles Neill, Murphy Yuezhen Niu, Eric Ostby, Andre Petukhov, John C. Platt, Chris Quintana, Eleanor G. Rieffel, Pedram Roushan, Nicholas C. Rubin, Daniel Sank, Kevin J. Satzinger, Vadim Smelyanskiy, Kevin J. Sung, Matthew D. Trevithick, Amit Vainsencher, Benjamin Villalonga, Theodore White, Z. Jamie Yao, Ping Yeh, Adam Zalcman, Hartmut Neven, and John M. Martinis. Quantum supremacy using a programmable superconducting processor. *Nature*, 574(7779):505–510, October 2019.

[10] Jay M. Gambetta, Jerry M. Chow, and Matthias Steffen. Building logical qubits in a superconducting quantum computing system. *npj Quantum Information*, 3(1):2, December 2017.

[11] Jens Koch, Terri M. Yu, Jay Gambetta, A. A. Houck, D. I. Schuster, J. Majer, Alexandre Blais, M. H. Devoret, S. M. Girvin, and R. J. Schoelkopf. Charge-insensitive qubit design derived from the Cooper pair box. *Physical Review A*, 76(4):042319, October 2007.

[12] T. P. Orlando, J. E. Mooij, Lin Tian, Caspar H. van der Wal, L. S. Levitov, Seth Lloyd, and J. J. Mazo. Superconducting persistent-current qubit. *Physical Review B*, 60(22):15398–15413, December 1999.

[13] Fei Yan, Simon Gustavsson, Archana Kamal, Jeffrey Birenbaum, Adam P Sears, David Hover, Ted J. Gudmundsen, Danna Rosenberg, Gabriel Samach, S Weber, Jonilyn L. Yoder, Terry P. Orlando, John Clarke, Andrew J. Kerman, and William D. Oliver. The flux qubit revisited to enhance coherence and reproducibility. *Nature Communications*, 7(1):12964, December 2016.

[14] Fei Yan, Youngkyu Sung, Philip Krantz, Archana Kamal, David K. Kim, Jonilyn L. Yoder, Terry P. Orlando, Simon Gustavsson, and William D. Oliver. Engineering Framework for Optimizing Superconducting Qubit Designs. *arXiv:2006.04130 [quant-ph]*, June 2020. arXiv: 2006.04130.

[15] Philip Krantz, Morten Kjaergaard, Fei Yan, Terry P. Orlando, Simon Gustavsson, and William D. Oliver. A Quantum Engineer's Guide to Superconducting Qubits. *Applied Physics Reviews*, 6(2):021318, June 2019. arXiv: 1904.06560.

[16] Alexandre Blais, Arne L. Grimsmo, S. M. Girvin, and Andreas Wallraff. Circuit quantum electrodynamics. *Reviews of Modern Physics*, 93(2):025005, May 2021.

[17] Peter Groszkowski, A Di Paolo, A L Grimsmo, A Blais, D I Schuster, A A Houck, and Jens Koch. Coherence properties of the 0- π qubit. *New Journal of Physics*, 20(4):043053, April 2018.

[18] Martin H Leib. *Many-Body Physics with Circuit Quantum Electrodynamics*. PhD thesis, Technischen Universität München.

[19] S.E. Rasmussen, K.S. Christensen, S.P. Pedersen, L.B. Kristensen, T. Bækkegaard, N.J.S. Loft, and N.T. Zinner. Superconducting Circuit Companion—an Introduction with Worked Examples. *PRX Quantum*, 2(4):040204, December 2021.

[20] B. D. Josephson. Possible new effects in superconductive tunnelling. *Physics Letters*, 1(7):251–253, July 1962.

[21] V. Bouchiat, D. Vion, P. Joyez, D. Esteve, and M. H. Devoret. Quantum Coherence with a Single Cooper Pair. *Physica Scripta*, T76(1):165, 1998.

[22] Philipp Aumann, Tim Menke, William D. Oliver, and Wolfgang Lechner. CircuitQ: An open-source toolbox for superconducting circuits. *arXiv:2106.05342 [quant-ph]*, June 2021. arXiv: 2106.05342.

[23] Morten Kjaergaard, Mollie E. Schwartz, Jochen Braumüller, Philip Krantz, Joel I.-J. Wang, Simon Gustavsson, and William D. Oliver. Superconducting Qubits: Current State of Play. *Annual Review of Condensed Matter Physics*, 11(1):369–395, March 2020.

[24] Karsten Flensberg, Felix von Oppen, and Ady Stern. Engineered platforms for topological superconductivity and Majorana zero modes. *Nature Reviews Materials*, 6(10):944–958, October 2021.

[25] Alexei Kitaev. Unpaired Majorana fermions in quantum wires. *Physics-Uspekhi*, 44(10S):131–136, October 2001. arXiv: cond-mat/0010440.

[26] Peter Brooks, Alexei Kitaev, and John Preskill. Protected gates for superconducting qubits. *Physical Review A*, 87(5):052306, May 2013. arXiv: 1302.4122.

[27] András Gyenis, Pranav S. Mundada, Agustin Di Paolo, Thomas M. Hazard, Xinyuan You, David I. Schuster, Jens Koch, Alexandre Blais, and Andrew A. Houck. Experimental Realization of a Protected Superconducting Circuit Derived from the $0 - \pi$ Qubit. *PRX Quantum*, 2(1):010339, March 2021.

[28] P. Kumar, S. Sendelbach, M. A. Beck, J. W. Freeland, Zhe Wang, Hui Wang, Clare C. Yu, R. Q. Wu, D. P. Pappas, and R. McDermott. Origin and Reduction of 1 / f Magnetic Flux Noise in Superconducting Devices. *Physical Review Applied*, 6(4):041001, October 2016.

[29] D. J. Van Harlingen, T. L. Robertson, B. L. T. Plourde, P. A. Reichardt, T. A. Crane, and John Clarke. Decoherence in Josephson-junction qubits due to critical-current fluctuations. *Physical Review B*, 70(6):064517, August 2004.

[30] A. Kou, W. C. Smith, U. Vool, R. T. Brierley, H. Meier, L. Frunzio, S. M. Girvin, L. I. Glazman, and M. H. Devoret. Fluxonium-Based Artificial Molecule with a Tunable Magnetic Moment. *Physical Review X*, 7(3):031037, August 2017.

[31] Mohamed Abdelhafez, Brian Baker, András Gyenis, Pranav Mundada, Andrew A. Houck, David Schuster, and Jens Koch. Universal gates for protected superconducting qubits using optimal control. *Physical Review A*, 101(2):022321, February 2020.

[32] E.T. Jaynes and F.W. Cummings. Comparison of quantum and semiclassical radiation theories with application to the beam maser. *Proceedings of the IEEE*, 51(1):89–109, January 1963. Conference Name: Proceedings of the IEEE.

[33] Bruce W. Shore and Peter L. Knight. The Jaynes-Cummings Model. *Journal of Modern Optics*, 40(7):1195–1238, July 1993.

[34] Christopher Gerry and Peter Knight. *Introductory Quantum Optics*. Cambridge University Press, Cambridge, 2004.